5-2024

Computational Fluid Dynamics Study of Perforated Monopiles

Mary Kathryn Walker
Florida Institute of Technology, mwalker2022@my.fit.edu

Recommended Citation

Walker, Mary Kathryn, "Computational Fluid Dynamics Study of Perforated Monopiles" (2024). *Theses and Dissertations*. 1447.
https://repository.fit.edu/etd/1447

Computational Fluid Dynamics Study of Perforated Monopiles

by

Mary Kathryn Walker

A thesis submitted to the Department of Ocean Engineering and Marine Sciences
of
Florida Institute of Technology
in partial fulfillment of the requirements
for the degree of

Master of Science
in
Ocean Engineering

Melbourne, Florida
May, 2024

We the undersigned committee hereby approve the attached thesis,
“Computational Fluid Dynamics Study of Perforated Monopiles”
by
Mary Kathryn Walker

Robert J. Weaver, Ph.D.
Associate Professor
Ocean Engineering and Marine Sciences
Major Advisor

Chungkuk Jin, Ph.D.
Assistant Professor
Ocean Engineering and Marine Sciences

Kelli Z. Hunsucker, Ph.D.
Assistant Professor
Ocean Engineering and Marine Sciences

Richard B. Aronson, Ph.D.
Professor and Department Head
Ocean Engineering and Marine Sciences

Abstract

Title: Computational Fluid Dynamics Study of Perforated Monopiles

Author: Mary Kathryn Walker

Advisor: Robert J. Weaver, Ph.D.

Monopiles are used in the construction of offshore wind turbines and typically have a design life of 25 to 50 years. Over their lifecycle, monopiles are exposed to a corrosive saltwater environment, facilitating a galvanic oxidation process that quickly degrades the structure. This process can be mitigated by coating the monopile in a protective barrier and implementing cathodic protection techniques. Historically, monopile designers assumed the interior of the pile would be completely sealed and the galvanic corrosion process would eventually consume all the available oxygen, halting the reaction. However, penetrations made in the pile wall for conduit often leaked and allowed fresh, oxygenated water to enter the interior space. New monopile designs are being researched that reconsider the interior space as an oxygenated environment where standard corrosion protection techniques can be more effectively applied. These new monopiles have perforations through the wall at intertidal or subtidal levels to allow fresh, oxygenated water to flow through the structure. These perforations can also reduce wave loads on the structure. The magnitude of the hydrodynamic load reduction depends on the size and orientation of the perforations. This research studied the applicability of computational fluid dynamics (CFD) in analysis of force reduction on monopiles in relation to size of a perforation and to analyze the effect of variation in approach angle of a given wave. To determine the force reduction on the monopile, theoretical 3D models were produced and tested using FLOW-3D® HYDRO with an unperforated monopile used as the control. After the theoretical data was collected, physical scale models with the same variety of perforations were tested using a wave tank to determine the validity of the theoretical models. The CFD simulations were found to be within 10% of the physical models and within 5% of previous research. After the physical and simulated models were validated, it was found that the size of the perforations has a distinct impact on the wave load reduction and testing for differing approach angles of a given wave could be conducted. The variation in approach angle was simulated by rotating the monopile in 15° increments. The data presented in this paper suggests that the orientation of the monopile is not statistically significant and should not be a design consideration for perforated monopiles. It is also suggested to continue the study on the size and shape of the perforations to find the balance between wave load reduction and structural stability.

Table of Contents

List of Figures

List of Tables

Chapter 1

Introduction

Offshore monopiles were originally designed to be completely sealed thereby creating an oxygen-deprived environment inside the monopile preventing galvanic corrosion. Galvanic corrosion occurs in seawater when a difference in potential along the metal's surface causes electricity pass through the metal. On a large steel structure such as a monopile, changes in electrical potential can develop due to differences in the available oxygen across the surface of the structure. The areas of the structure with more oxygen become relatively positive and drive the cathodic chemical reaction shown below (Goodisman, 2001).

$$O_{2_g} + 4H^+_{(aq)} + 4e^- \rightarrow 2H_2O_{(l)} \tag{1}$$

Where,

O = Oxygen

H = Hydrogen

e = electron

As the cathodic reaction occurs using up the available oxygen the following reaction takes places at the anode (Goodisman, 2001).

$$Fe(s) \rightarrow \ 2Fe^{2+}_{(aq)} + 2e^- \tag{2}$$

Where,

Fe = Iron

e = electron

The sealed monopile design philosophy that is used for the piles of offshore oil platforms takes advantage of the anaerobic environment that occurs because of the galvanic corrosion reaction (EQ. 1). However, there is a major difference between monopiles used for oil platforms and those used for offshore wind applications as pointed out by corrosion research conducted by Hilbert, et al. (2011). The study focused on inspecting an existing 5 to 10-year-old wind farm with thirty-six monopiles for evidence of corrosion and oxygen in the interior of the monopiles. Due to the J-tube conduit needed to transport electricity from the turbine to shore, Figure 1, only 8% of the monopiles used for wind turbines were watertight. The other 92% of monopiles were letting in tiny amounts of oxygenated seawater into the interior of the monopile.

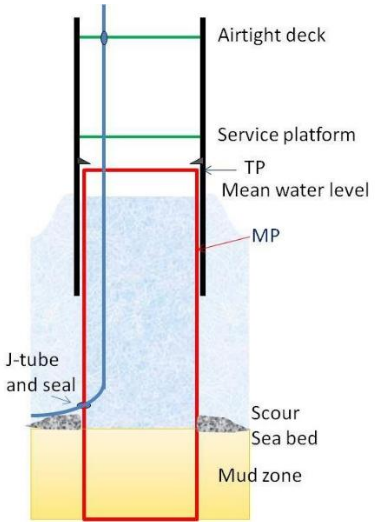

Figure 1: Overview sketch of typical monopile (MP) foundation and transition piece (TP) design with an internal j-tube (Hilbert et al., 2011)

According to Hilbert, et al. (2011) the maximum corrosion rates in an airtight monopile structure is around the water line is an estimated 0.2 mm/year locally. However, the slight ingress of oxygenated water increases this rate to a maximum local rate of 0.5 mm/year around the water line. This increase is due to low oxygen or anoxic environment but not completely oxygen deprived which allows for galvanic corrosion to continue assisted by a flourish in microorganisms. The relationship between pitting depth vs. exposure period and oxygen conditions at the surface of the monopile, Figure 2, show that the depth of corrosion found on an oxygenated surface not influenced by microbiological growths is less than the corrosion depth in an anoxic environment with microbiological growth. For existing offshore monopiles using the current design, the assumption of an aerobic interior environment requires more frequent inspections to be conducted than if the monopiles were able to be sealed as designed.

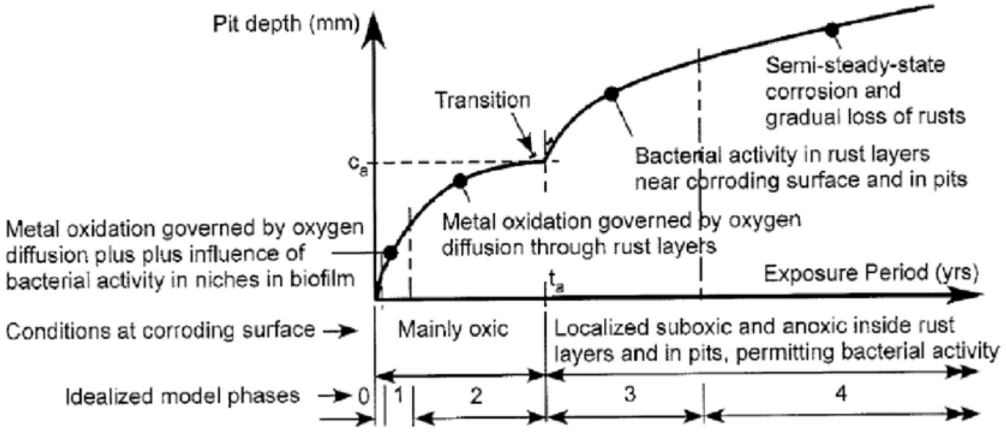

Figure 2: "Idealised model for growth in maximum pit depth as a function of exposure period, with brief summaries of rate controlling mechanism for each phase" (Hilbert, et al., 2011)

Delwiche & Tavares (2017) attempted to solve the low oxygenation on the interior of the monopile by perforating the monopiles with small holes around the j-tubes at the bottom of the monopile. The flushing caused by the perforations would allow for traditional methods of corrosion control and mitigation to be used to limit corrosion for the service life of the monopile. Monica Maher and Dr. Geoffrey Swain of Florida Institute of Technology presented further research on perforated monopiles at the 2018 OCEANS conference. In Maher, et al. (2018) the added perforations were shown to increase the amount of dissolved oxygen in the water and increase the pH of the water on the monopile's interior, as seen in Table 1 below.

Table 1: Dissolved Oxygen and pH on Interior of Monopiles after 14 Days of Deployment (Maher, et al., 2018)

Pipe Treatment	YSI Probe Measurements		
	DO %	DO mg/L	pH
Sealed, cathodic protection	12.8	0.99	7.06
Perforation, cathodic protection	97.2	7.73	8.31
Sealed, freely corroding	2.2	0.17	7.88
Perforated, freely corroding	98.4	7.79	8.31
Ambient seawater	97.3	7.74	8.32

These perforations can also serve another purpose important to monopile design by reducing hydrodynamic loads. This application has been recently explored by 2 papers: “Wave Load Mitigation by Perforation of Monopiles” by Andersen, et al. (2020) and “Perforation of Monopiles to Reduce Hydrodynamic Loads and Enable use in Deep Waters” by Ploeg (2021). Both papers expand on the analysis of perforated monopiles in relation to the mitigation of hydrodynamic loads. As such they reach the same conclusion; wave loads reduce as perforation size increases.

The research conducted by Andersen, et al. (2020) generated 1:80 scale models of a reference and a perforated monopile. The perforation geometry consisted of ovular holes spaced at 30° about the center of the monopile as shown in Figure 3 below.

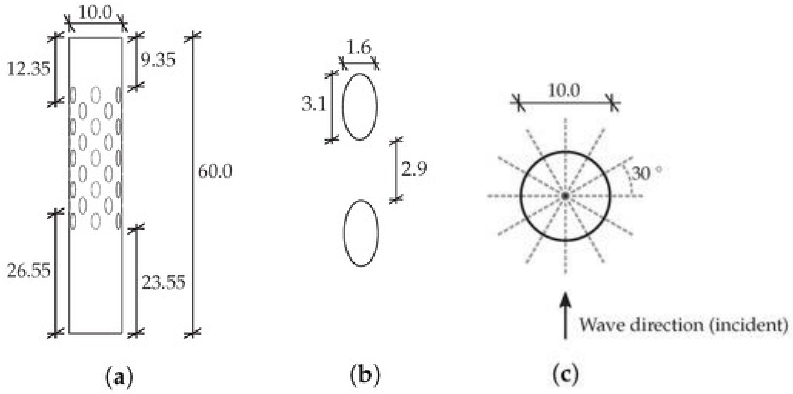

Figure 3: Perforated Monopile. All measurements are in meters (Andersen, et al., 2020)

The 1:80 scale model of the perforated and reference monopile were placed in a wave tank with the setup shown in Figure 4. Perforated plates were used to limit tangential waves while both wave and strain gauges collected data on incident and reflected waves and horizontal force. A total of 16 waves were tested and the observed wave heights for the regular wave states with and without the model in place were recorded, Table 2. The observed wave heights around the monopile are smaller than those observed without the model in place.

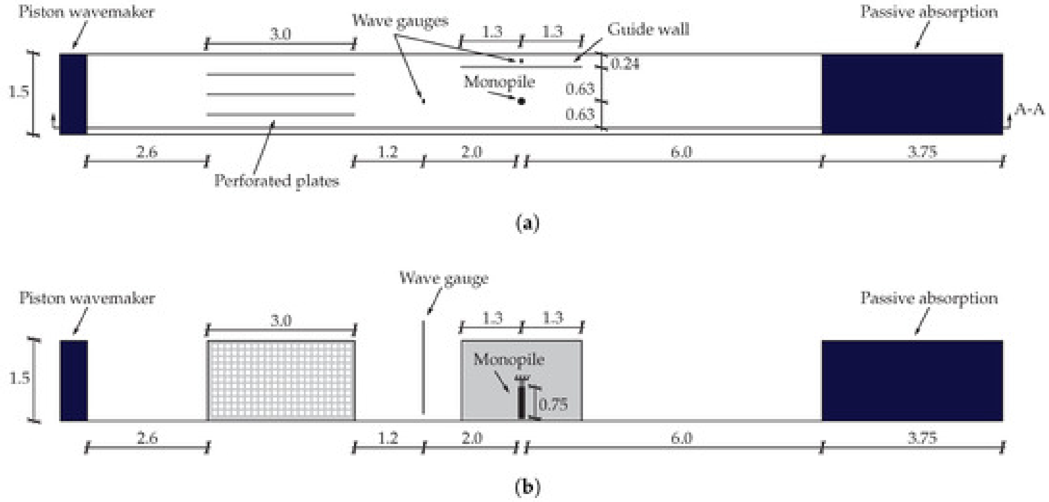

Figure 4: "Setup of wave flume used in the experiments" (Andersen, et al., 2020)

Table 2: “Measured wave heights for the regular sea state tests with and without the model in place” (Andersen, et al., 2020)

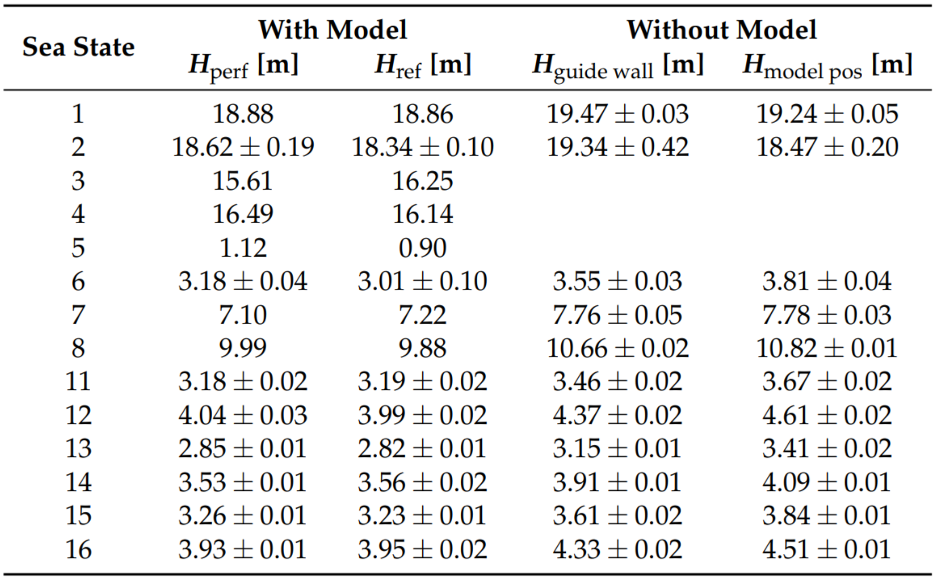

Sea State	With Model		Without Model	
	H_{perf} [m]	H_{ref} [m]	$H_{\text{guide wall}}$ [m]	$H_{\text{model pos}}$ [m]
1	18.88	18.86	19.47 ± 0.03	19.24 ± 0.05
2	18.62 ± 0.19	18.34 ± 0.10	19.34 ± 0.42	18.47 ± 0.20
3	15.61	16.25		
4	16.49	16.14		
5	1.12	0.90		
6	3.18 ± 0.04	3.01 ± 0.10	3.55 ± 0.03	3.81 ± 0.04
7	7.10	7.22	7.76 ± 0.05	7.78 ± 0.03
8	9.99	9.88	10.66 ± 0.02	10.82 ± 0.01
11	3.18 ± 0.02	3.19 ± 0.02	3.46 ± 0.02	3.67 ± 0.02
12	4.04 ± 0.03	3.99 ± 0.02	4.37 ± 0.02	4.61 ± 0.02
13	2.85 ± 0.01	2.82 ± 0.01	3.15 ± 0.01	3.41 ± 0.02
14	3.53 ± 0.01	3.56 ± 0.02	3.91 ± 0.01	4.09 ± 0.01
15	3.26 ± 0.01	3.23 ± 0.01	3.61 ± 0.02	3.84 ± 0.01
16	3.93 ± 0.01	3.95 ± 0.02	4.33 ± 0.02	4.51 ± 0.01

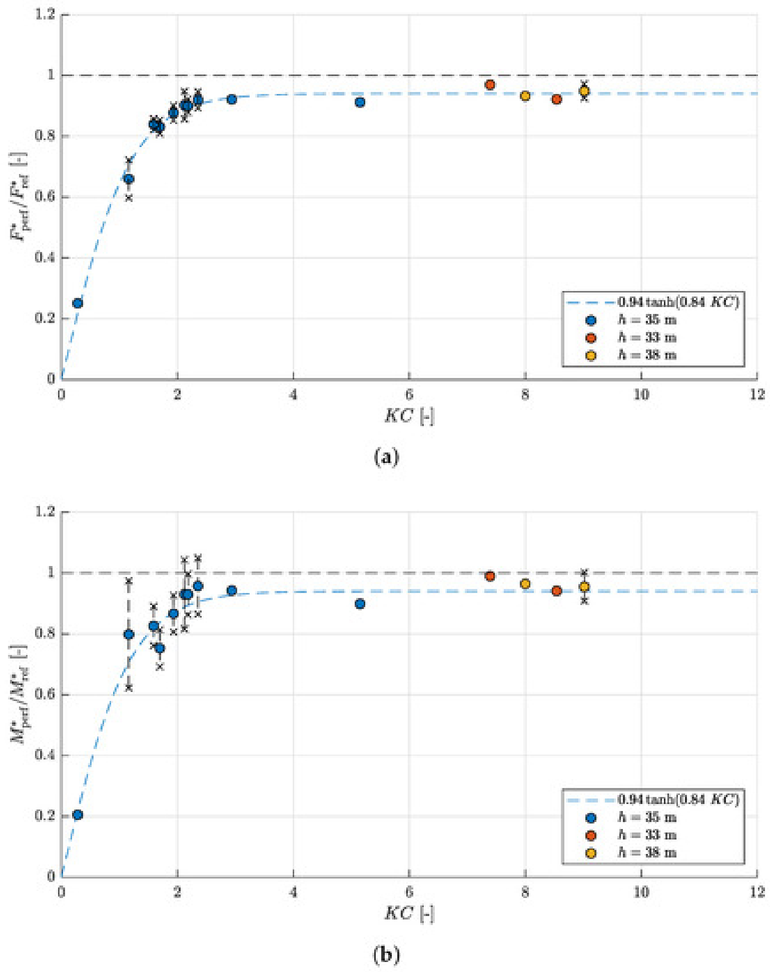

Figure 5: "Load reduction for different Keulegan-Carpenter (KC) numbers and water level... (a) Normalized resulting force... (b)Normalized mudline moment" (Andersen, et al., 2020)

Both the resulting force and mudline moment decreases for all KC numbers by an average of 5%, Figure 5. The most significant decrease is seen for KC numbers less than 2. The larger force reductions at low KC numbers are a result of the inertia component dominating in force (Chakrabarti, 2003). The inertia component of force is reduced for the perforated monopile when compared to the reference monopile, Figure 6.

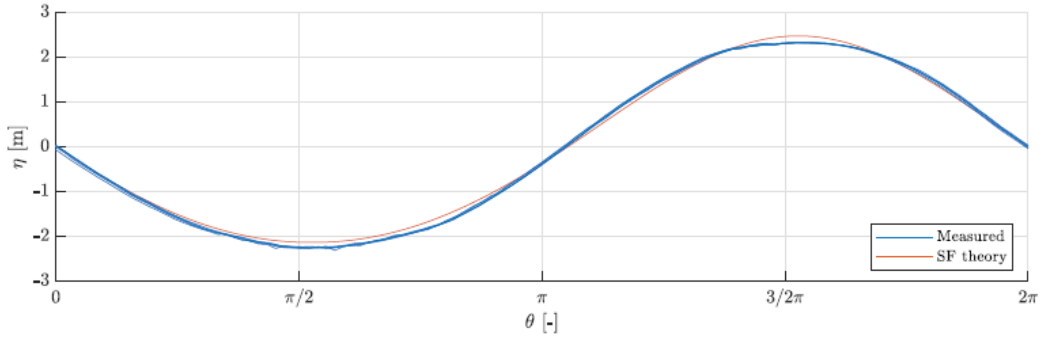

(a)

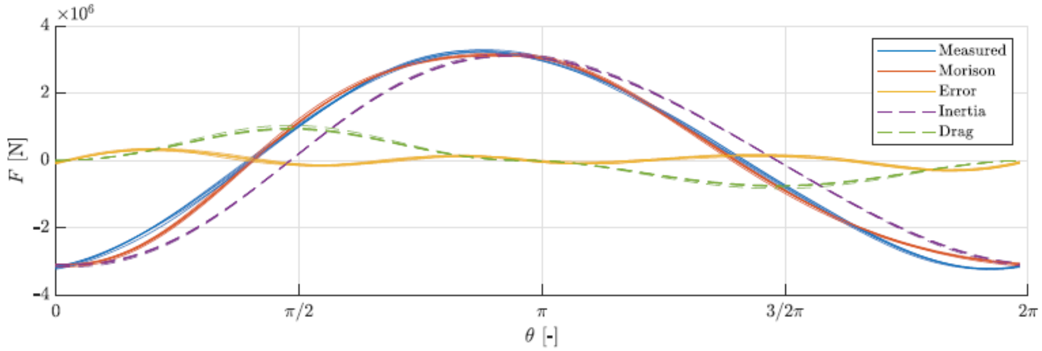

$C_M = 1.96 \pm 0.02$ and $C_D = 5.01 \pm 0.24$

(b)

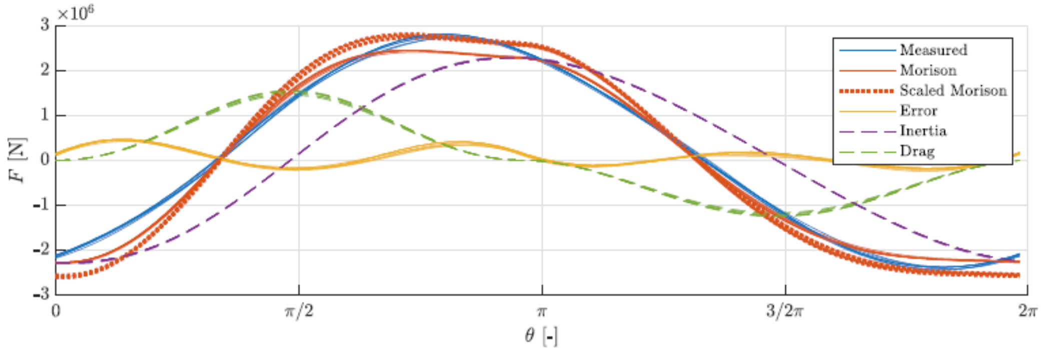

$C_M = 1.67 \pm 0.02$ and $C_D = 7.32 \pm 0.29$

(c)

Figure 6: “Surface elevations and force histories for sea state 12; H = 4.6m, T = 10.3s, h = 35m, KC =1.56. Wave heights are measured at the model location without the model in place. Force coefficients are given as the mean values +/- one standard deviation. (a) Surface elevation at model location. (b) Reference monopile. (c) Perforated monopile

Anderson, et al. (2020) concludes that the greatest force reduction of peak loads is for sea states 5 and 6 with the smallest KC numbers of the regular sea states tested. However, it is noted that stress concentrations increase when using perforations, so although the hydrodynamic forces are reduced “the fatigue lifetime may not increase” (Andersen, et al., 2020).

While Andersen, et al., (2020) does not consider the additional stress concentration Ploeg (2021) does along with testing for two additional perforation geometries. Ploeg used COMSOL Multiphysics®, a 3D CFD modelling software, to compute stresses on the reference IEA 15 MW monopile on 12 sea states for each of the three perforation geometries (Gaertner, et al., 2020). The geometry of the perforations can be seen in Figure 7 below.

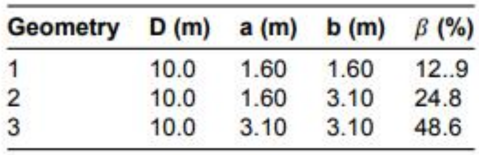

Geometry	D (m)	a (m)	b (m)	β (%)
1	10.0	1.60	1.60	12..9
2	10.0	1.60	3.10	24.8
3	10.0	3.10	3.10	48.6

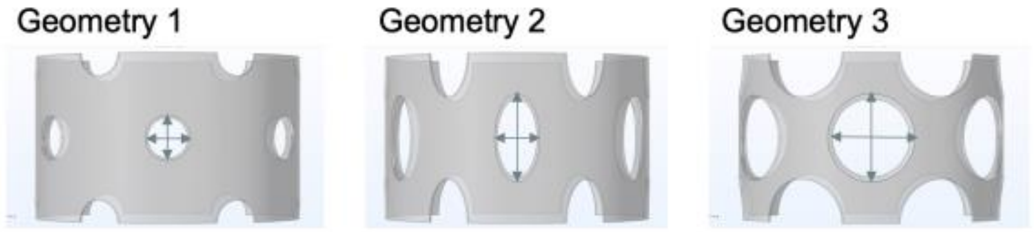

Figure 7: "Geometry dimensions, where D is monopile diameter, a is perforation width and b is perforation height" (Ploeg, 2021)

The geometries affect the force mitigation capability of the perforated monopiles. The increase in perforation size results in an increase in force reduction, Figure 8.

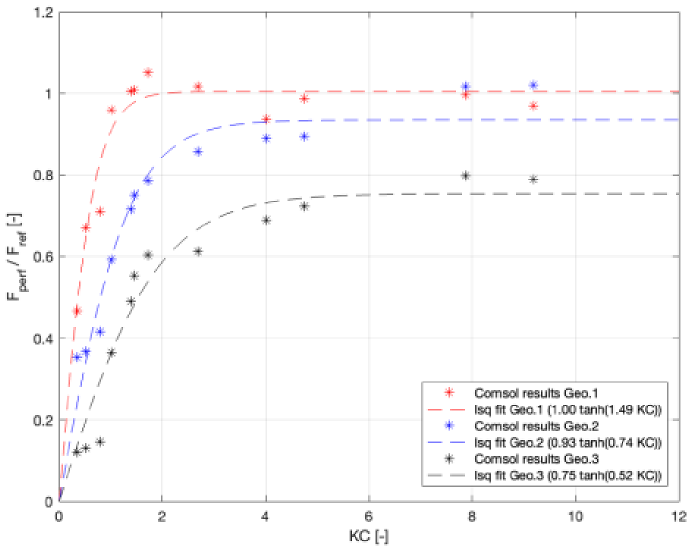

Figure 8: Individual data points and resulting lines of best fit for each perforation geometry (Ploeg, 2021)

While the force decreases with an increase in perforation size, the largest perforation, geometry #3, causes extreme stress concentrations on the remaining material. Geometry #2 showed the largest load reduction while the stress concentrations remain within the allowable fatigue limits per Det Norske Veritas (DNV) guidelines (DNV, 2011), Figure 9.

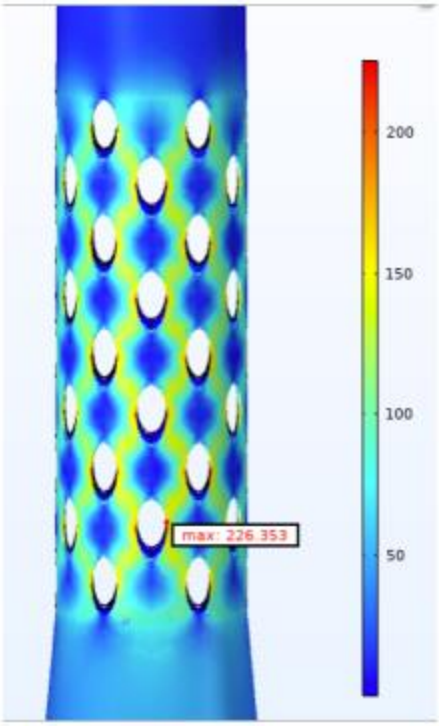

Figure 9: "Stresses around perforations... for geometry 2..., stresses are in MPA" (Ploeg, 2021)

Both Andersen, et al. (2020) and Ploeg (2021) conclude that perforations reduce forces due to wave loads; however, the perforations will increase stress loads in the material surrounding it. Andersen, et al. (2020) recommend a numerical and stress analysis be conducted with variation on geometry number and spacing of holes. Ploeg (2021) recommends the examination of elongated elliptical perforation, maximum pile porosity vs minimizing stress concentrations and explore structural reinforcement to be able to increase porosity further.

Flow Around a Monopile

As described in Christiansen (2020), 3 non-dimensional numbers are needed to describe the flow around a cylinder and to understand the numerical models that may be used to compute the forces on a monopile. The first number was developed by Osbourne Reynolds in 1883 (Journee, 2001). Reynolds conducted several experiments using dyed water to observe flow through a glass tube at the bottom of a filled container, Figure 10.

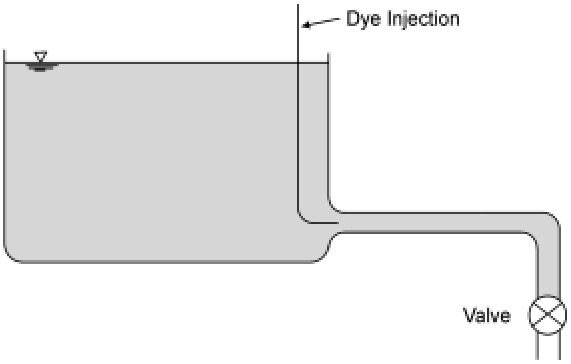

Figure 10: Reynolds' Experiement Setup (Journee, 2001)

By observing how the dye traveled through the glass tube Reynolds was able to observe the streamlines formed by the flow and deducted the following: the flow is initially linear, the rate of flow along the edges of the tube is less than that through the center and that the flow eventually becomes irregular. By using the valve at the end of the tube to change the opening size, Reynolds controlled the fluid's velocity. Reynolds observed that an increase in velocity caused the flow to become turbulent closer to the beginning of the tube and be continuing to vary the velocity he could change where in the tube the flow became turbulent. The relation shown below was developed based on the conducted experiments.

$$Rn = \frac{V * D}{\upsilon} = \frac{V * L}{\upsilon} \tag{3}$$

Where,

Rn = Reynolds Number

V = Flow Velocity

D = Pipe Diameter

L = Characteristic Length

υ = Kinematic Viscosity of the Fluid

Reynolds’ initial equation was designed for flow through pipes, as such for flow around structures a characteristic length (L) is used in place of pipe diameter (D). The characteristic length (L) is described as the shortest distance around the structure. For example, the characteristic length of a solid sphere is its diameter. As Reynolds number is the relation of the kinematic forces to viscous forces, it describes the flow as turbulent or laminar (Elger, 2022).

The next number was developed by Robert Edmund Froude as a relation between inertia and gravity forces as a method to scale models and is described by the equation below (Journee, 2001).

$$Fn = \frac{V}{\sqrt{gL}} \tag{4}$$

Where,

Fn = Reynolds Number

V = Flow Velocity

g = Gravity

L = Characteristic Length

Both Reynold’s number and Froude number may be used in scaling models for numerical or experimental testing. However, both methods of scaling have their uses. Reynolds scaling is important when focusing on pipe flow or wake formation behind a structure (Journee, 2001). Froude number scaling is important when gravity forces are dominant, such as when dealing with the free water surface (Journee, 2001). As such Froude number scaling is commonly used for experimental modeling of monopiles in wave tanks as seen by Shi, et al. (2023), Andersen, et al. (2020) and Tang, et al. (2020) and the Froude scaling laws of similitude can be seen in Table 3 below.

Table 3: Froude Scaling Laws of Similitude (Shi, et al., 2023)

Parameter	Dimension	Similarity Relation
Length	L	λ
Mass	M	λ^3
Velocity	LT^{-1}	$\lambda^{1/2}$
Acceleration	1	1
Time	T	$\lambda^{1/2}$
Force	MLT^{-2}	λ^3
Moment	ML2T-2	λ^4

The third non-dimensional number was developed by Garbis Keulegan and Lloyd Carpenter by "investigating the inertia and drag coefficients of cylinders in sinusoidal currents" (Christensen, 2020). By measuring forces experienced by the monopile and comparing it with the max horizontal velocity of the wave Keulegan and Carpenter were able to derive the inertia and drag coefficients and found it related to their non-dimensional parameter or KC number as shown below (Keulegan, et al., 1958).

$$KC = \frac{TU_m}{D} \tag{5}$$

Where,

KC = Keulegan-Carpenter Number

T = Wave Period

U_m = Max Horizontal Velocity

D = Diameter of Piling/Characteristic Length

Lower Keulegan-Carpenter number waves produce forces on cylindrical structures that are dominated by the inertia coefficient, Figure 12 (Sarpkaya, 1976). As the KC number increases the drag coefficient increases in dominance and the relative force reduction between a reference and perforated monopile shown in previous research decreases.

Different wave force theories should be used to accurately describe the force on an offshore structure depending on the slenderness of the structure in relation to the wavelength and the steepness of the wave as seen in Figure 11.

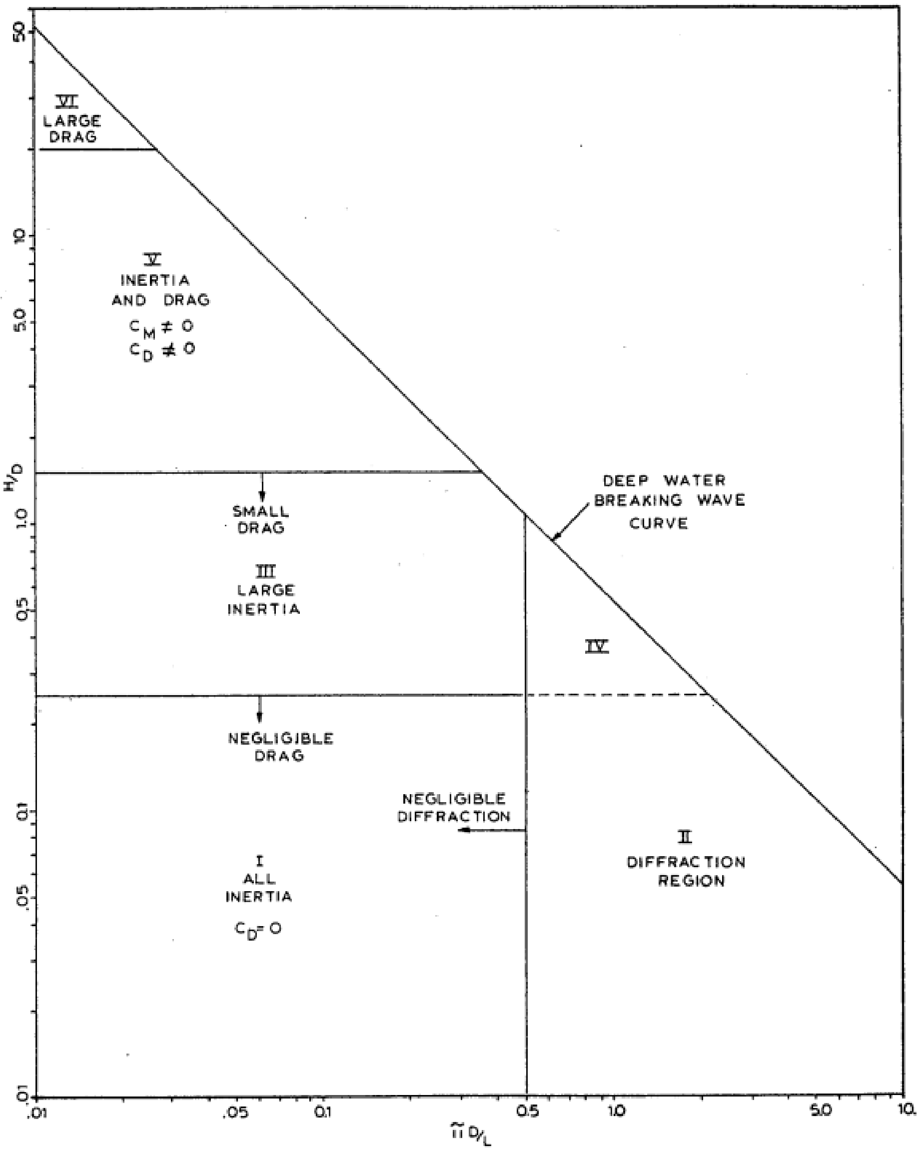

Figure 11: "Regions of Application of Wave-Force Formulas for a Vertical Cylinder" (Chakrabarti, 2003)

Several key regions can be pulled from Figure 11: Inertia & Drag, Large Inertia, All Inertia, and Diffraction. The differing wave force theories can be assigned to each of the regions. The first is Morison's equation for the inertia and drag region. Morison developed the following equation to predict wave forces on exposed vertical piles (Morison, et al., 1950).

$$F(t) = \frac{\pi}{4}\rho C_m D^2 \dot{v}(t) + \frac{1}{2}\rho C_D D v(t)|v(t)| \tag{6}$$

Where,

F(t) = Morison Force at a Given Time

C_m = Dimensionless Inertial Force Coefficient

C_D = Dimensionless Drag Force Coefficient

D = Diameter of Cylinder

v (t) = Water Particle Velocity

$\dot{v}$ (t) = Water Particle Acceleration

There are multiple ways to estimate the dimensionless force coefficients C_m and C_D from experimental data (Journee, 2021). The first is Morison's method where he determined the coefficients based on the knowledge that at the maximum velocity the acceleration is zero and vice versa. This yields the following equations:

$$C_m = \frac{4 * F(t_1)}{\pi \rho D^2 \dot{v}(t_1)} \tag{7}$$

$$C_D = \frac{2 * F(t_2)}{\rho v(t_2)|v(t_2)|} \tag{8}$$

Where,

t_1 = Time when v = 0 and $\dot{v}$ = maximum

t_2 = Time when v = maximum and $\dot{v}$ = 0

Although this method is simple it lacks accuracy as a small error in the velocity record can cause a significant phase error. The inaccuracy can be limited by averaging the coefficients over multiple wave periods. Another way to limit the inaccuracy is by using the least squares method which uses the minimization of a residual for various values of C_m and C_D. The residual function is given by:

$$R(C_m, C_D) = \int_0^T \left(F(t)_{measured} - F(t, C_m, C_D)_{completed}\right)^2 dt \tag{9}$$

The only fault with this method is that it’s possible to find multiple solutions that minimize the residual. This can be limited by setting the partial derivatives of the residual function equal to zero.

Typical values for C_m and C_D have been suggested by Clauss in 1992 for ranges of Reynolds and KC numbers (Table 4) and by Sarpkaya in 1981 for ranges of β (EQ. 10) and KC (Figure 12). Where β is defined as being equal to Re/KC = $D^2/\upsilon T$ Some of the most widely accepted values are from DNV (1989), as shown in Figure 13, and are suggested for design use.

Table 4: Morison Coeffiecients Suggest by Clauss, 1992

	$Rn < 10^5$		$Rn > 10^5$	
KC	$\mathbf{C}_D$	$\mathbf{C}_M$	$\mathbf{C}_D$	$\mathbf{C}_M$
< 10	1.2	2.0	0.6	2.0
$\geqslant 10$	1.2	1.5	0.6	1.5

$$\beta = \frac{Re}{KC} = \frac{D^2}{\upsilon T} \tag{10}$$

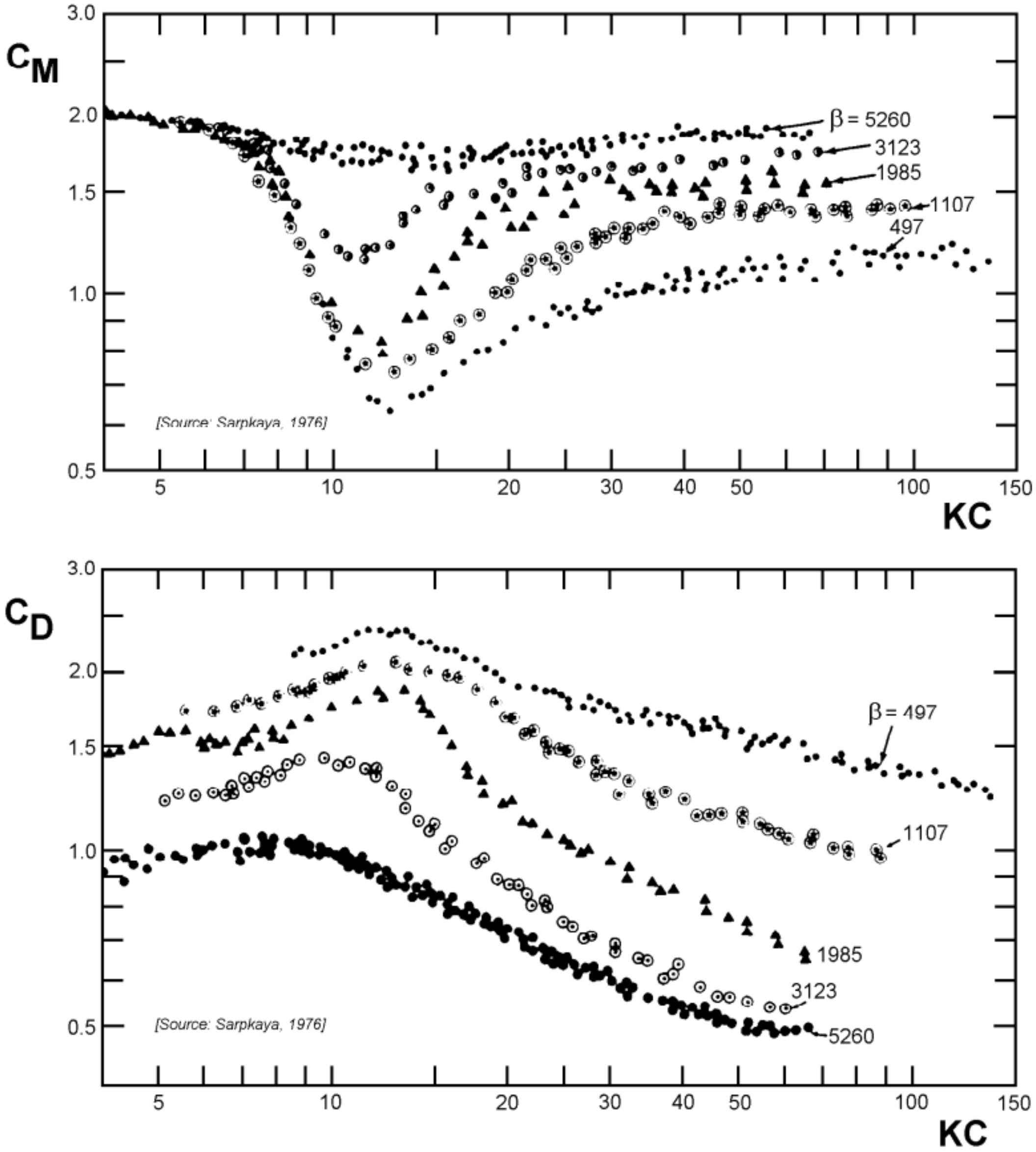

Figure 12: Associated drag and inerita coefficients for cylinders given beta value and KC number (Sarpkaya, 1976)

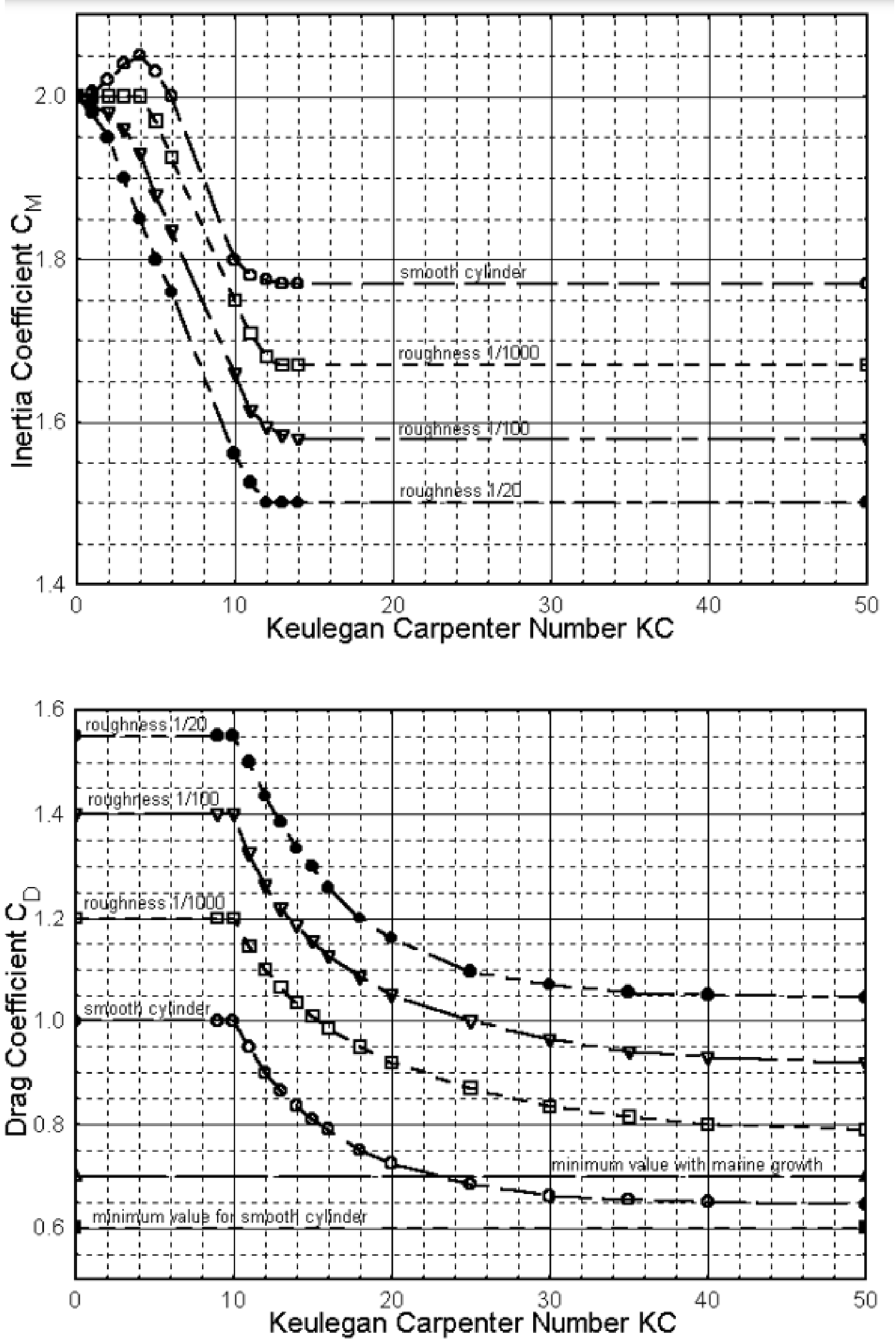

Figure 13: Associated drag and inerita coefficients for cylinders given roughness and KC number (DNV, 1989)

Next is the large inertia and all inertia sections of the wave regime which includes slender structures. The force for both regions can be calculated using Froude-Krylov force as given by the equations below (Journee, 2001).

$$F_x = C_H \iint_{Sb} P n_x d_x \tag{11}$$

$$F_z = C_V \iint_{Sb} P n_z d_z \tag{12}$$

Where,

C_H = Dimensionless Horizontal Force Coefficient

C_V = Dimensionless Vertical Force Coefficient

P = Pressure = $-\rho \frac{\partial \phi_I}{\partial t}$

n_x = Normal Vector in the X Direction

n_z = Normal Vector in the Z Direction

S_b = Submerged Body Volume

For the large inertia section has a small drag component that can be accounted for by adding the drag component of Morison's equation. The KC number may be used to determine if the drag component is necessary via the following relation:

$$\frac{F_{drag}}{F_{inertia}} = \frac{1 * C_D}{\pi^2 C_M} * KC \tag{13}$$

From the relation KC numbers can describe the relationship between the inertia and drag component of Morrison's equation. For KC < 3 the inertia force is dominant and drag can be neglected. For 3 < KC < 45 both inertia and drag are important and finally for KC > 45 drag force is dominant and inertia may be neglected.

Finally, the diffraction region from Figure 11 is calculated by the methodology carried out by MacCamy and Fuchs (1954) in their analysis of a bottom mounted vertical cylinder. By applying 5 boundary conditions to the governing Laplace equation and applying the Jacob-Angler expansion and Bessel/Hankel functions the following equations were extrapolated (MacCamy and Fuchs, 1954).

$$P(a,\theta,z) = -\rho g z - \rho \frac{\delta \phi_D}{\delta t}\,|_{r=a}$$

$$= -\rho g z - \rho g H \frac{\cosh\big(k(z+h)\big)}{\cosh(kh)} \left[\sum_{m=0}^{\infty} \frac{iB_m \cos(m\theta)}{\pi k a {H_m}^{(1)'}(ka)}\right]^{e^{-i\omega t}} \qquad (14)$$

$$F_x = \frac{-2pgHah}{ka} \frac{1}{\sqrt{J_1^{\prime(2)}(ka) + Y_1^{\prime(2)}(ka)}} \qquad (15)$$

Where,

P = Pressure

ϕ_D = Diffracted Velocity Potential

θ = Angle around the Cylinder

a = Radius of Cylinder

z = Depth

h = Water Depth

H = Wave Height

g = Gravitational Acceleration

k = 2π/L

L = wavelength

J_m = Bessel Function of the First Kind of Order m

Y_m = Bessel Function of the Second Kind of Order m

H_m = Hankel Function of the First Kind of Order m

$B_m = 0$ if $m = 0$, $2i^m$ if $m \geq 1$

While the diffraction region of Figure 12 is for larger diameter structures in relation to wavelength than those used in this research, the application of MacCamy and Fuchs (1954) solution is best suited as a numerical solution to check observed results. Morison’s equation and Froude-Krylov force are not suited to this application as they require the estimation of inertia and drag coefficients to determine applied force. Typical inertia and drag coefficients range from roughly 2.5 to 0.6, however those determined by Anderson, et al. (2020) varied between 0.98 and 2.01 for the inertia coefficient but 1.1 to 14.96 for the drag coefficient. As such estimating the drag coefficient using typical guidelines would not yield accurate results.

As the noted difference in force was due to a decrease in the inertia coefficient between a reference and perforated monopile the understanding of Morisons and Froude-Krylov theory is necessary for interpreting any observed results.

Chapter 2

Methodologies

This study aims to investigate how the incident wave direction influences the mitigation of hydrodynamic loads on a perforated monopile. The change in direction of the incident wave is modeled by rotating the monopile about its center. The modeling of rotation vs. force reduction is conducted using computational fluid dynamics (CFD) simulations and scaled physical models in a wave tank. The scaled models will serve the additional purpose of validating the CFD simulation results. Both the physical model and CFD simulation were compared with Andersen, et al. (2020) and Ploeg (2021) for validation.

Experimental Design

A scaled model was subjected to hydrodynamic forces in the wave tank at Florida Institute of Technology to accurately analyze and verify results from a CFD analysis. The wave tank's physical dimensions measure 8.23 m (27 ft) long, 0.56 m (22 in) wide, and 0.91 m (3 ft) tall. The model was based on the IEA 15MW reference turbine (Gaertner, et al., 2020) with a diameter of 10m in the splash zone with a depth ranging from 33m to 38m. Based on the size of the wave tank a 1:80 scaling was used for the physical model. Froude laws of similitude are used to scale the monopile and wave conditions as recommended by DNV-RP-C203: Fatigue Design of Offshore Structures (2019). The resultant scaled dimensions of the monopile are 12.5 cm (5 in.) in diameter and a height of 68.75 cm (27.07 in).

In total 4 scaled models were tested including the unperforated reference monopile and 3 models with perforations with the sizing provided in Table 5 below. The perforations were cut at a 30-degree offset alternating columns of four and five perforations, Figure 3. These geometries were selected to allow for comparison with Andersen, et al. (2020) and Ploeg (2021).

Table 5: Experimental Perforation Geometries

Perforation Geometry Number	a (m)	Scaled a (cm)	b (m)	Scaled b (cm)
1	1.6	2	1.6	2
2	1.6	2	3.1	3.875
3	3.1	3.875	3.1	3.875

The direction of approaching wave was varied throughout the tests by rotating the piles in the wave tank by 15 degree increments between each test starting at 0 degrees and ending at 45 degrees. Three test waves were selected from those used in Andersen, et al. (2020) and Ploeg (2021). The water depth (h) significant wave height (H_s) and peak period (T_p) for the 3 selected waves are shown in Table 6 below. The selected test states for the scaled experiments allow for a constant water depth across all experiments, comparability with Ploeg (2021). Ploeg (2021) tested only 9 of the 16 test states outline by Andersen, et al. (2020). The limitations of the wave tank at Florida Tech were also a consideration as the wave tank motor has a maximum frequency of 1.5 Hz or a minimum period of 0.66 seconds. The frequency limits the selection to waves with unscaled periods longer than 5.96 seconds. The three selected waves are also in the large inertia region which showed the greatest load reductions in both Andersen, et al. (2020) and Ploeg (2021). In total, 12 tests was conducted for each model, including the 4 rotations and 3 test waves. 3 runs were conducted for each setup of a given model to limit variations in the waves produced by the wave maker.

Table 6: Tested Sea States for Experimental Model with Scaled Model Values

Wave Test Number	Andersen Test Number	Sea State (Beaufort)	h(m)	h(cm), Scaled	H_s(m)	H_s(cm), Scaled	T_p(s)	T_p(s), Scaled	KC
1	6	6-7	35	43.75	3.80	4.75	7.30	0.816	1.16
2	8	10	35	43.75	10.80	13.5	15.10	1.69	5.15
3	13	7	35	43.75	3.40	4.25	20.40	2.28	2.12

The hydrodynamic forces were measured by a load cell attached to the monopile's interior during testing. The force gauge is formed by four strain gauges on an aluminum bar connected in a wheatstone bridge design (Lahlou, 2020). The wheatstone bridge design allows for the measurement of minor changes in the voltage from the strain gauges (Teja, 2021). The strain gauges and aluminum bar form the load cell. The voltage from the load cell is the input into the data collection system, which is comprised of a HX711 ADC, Arduino Uno and a 12v battery and may be seen in Figure 14 below.

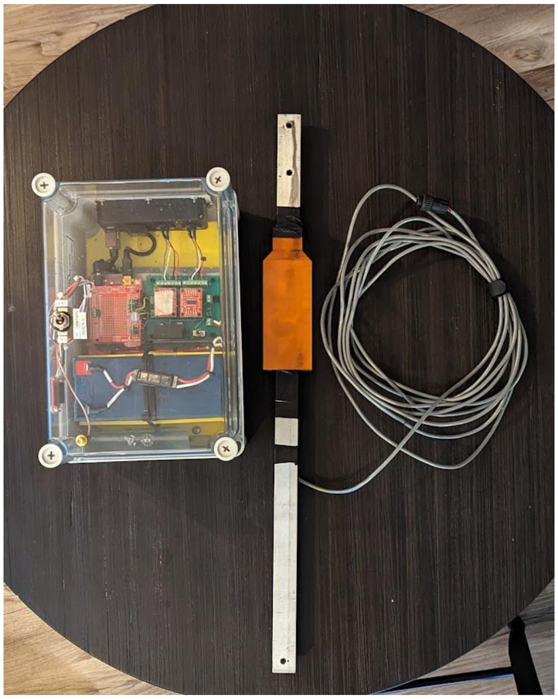

Figure 14: Load Cell and Data Collection System

The HX711 ADC supplies an excitation voltage to increase the resolution of measurable voltages. The voltage is then input into the Arduino Uno for processing and transmission via USB as a serial output to the program CoolTerm. CoolTerm is a serial port terminal which facilitates the exchange of data from hardware connected serial ports. Prior to model setup the load cell is calibrated with known loads to associate the output voltage with a load in newtons. The calibration was comprised of the following weights: 0g, 50g, 100g, 200g, 300g, 400g, 500g, 600g, 1000g. The raw data, Figure 14, develops a linear relation between strain and applied force, Figure 16, by using a least squares reduction function.

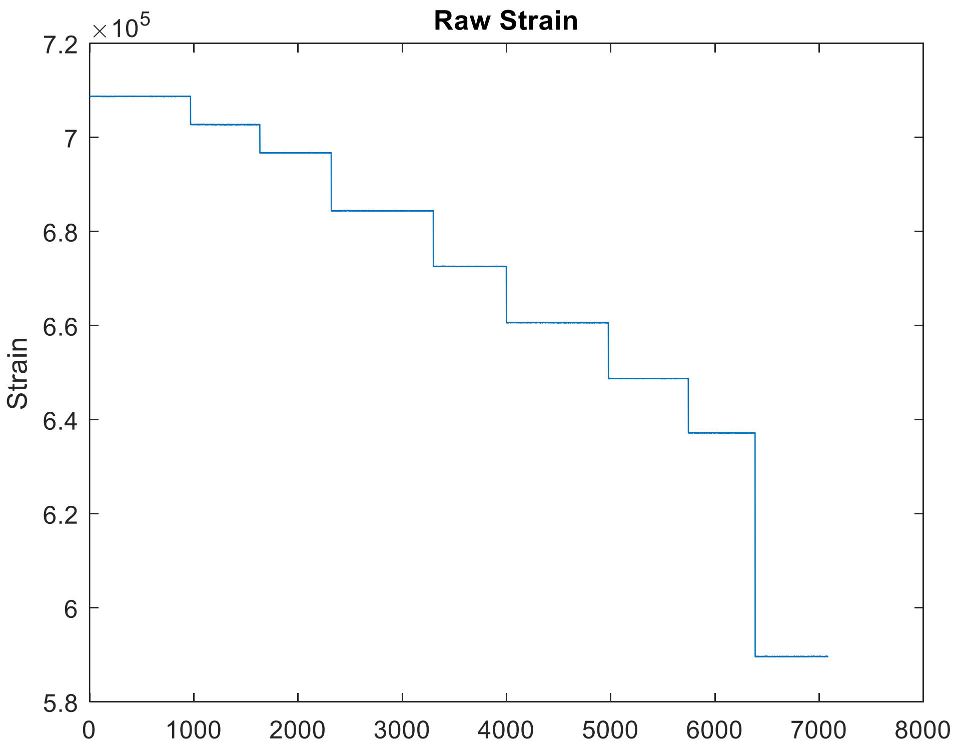

Figure 15: Raw strain output from load cell during calibration

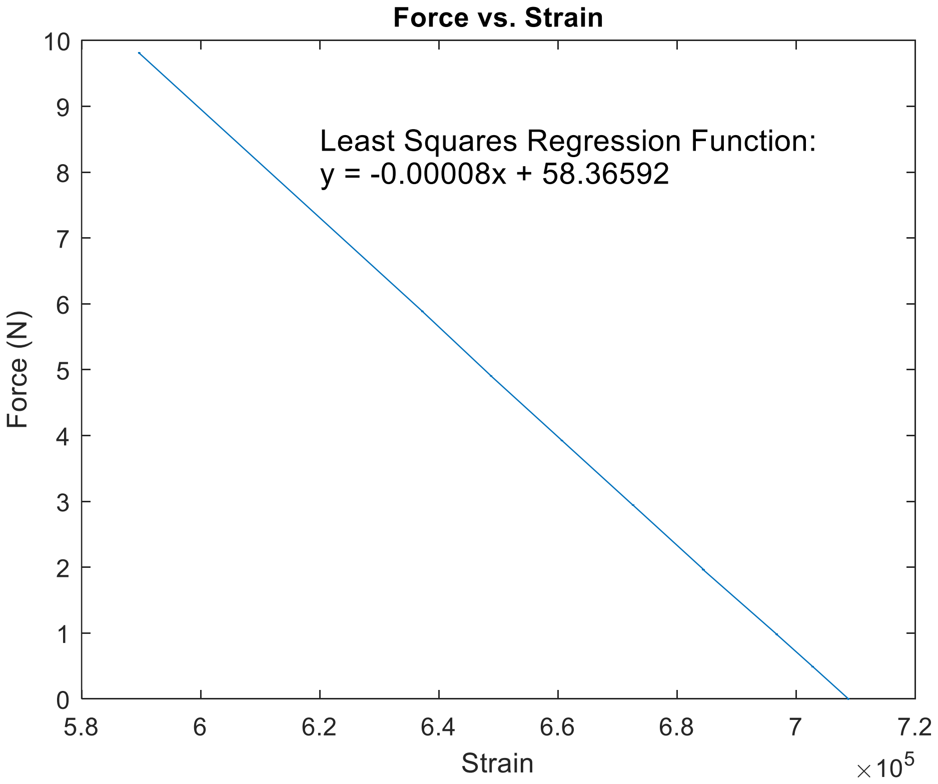

Figure 16: Force vs. Strain relationship for load cell with associated least squares regression function

The center of force beneath the mean water level varies in elevation as a wave passes the monopile. Using the MacCamy and Fuchs (1954) approach, the center of force at the peak and minimum hydrodynamic loads were determined for each test wave, Table 6. From the determined center of forces for each wave a list of points encapsulating the center of forces was formulated to calibrate the load cell. The center of forces for each wave and the calibration points were marked on a perforated monopile, Figure 17. The load cell was calibrated with point loads at each of the calibration points on the monopile from -3 cm to -24 cm from the mean water level.

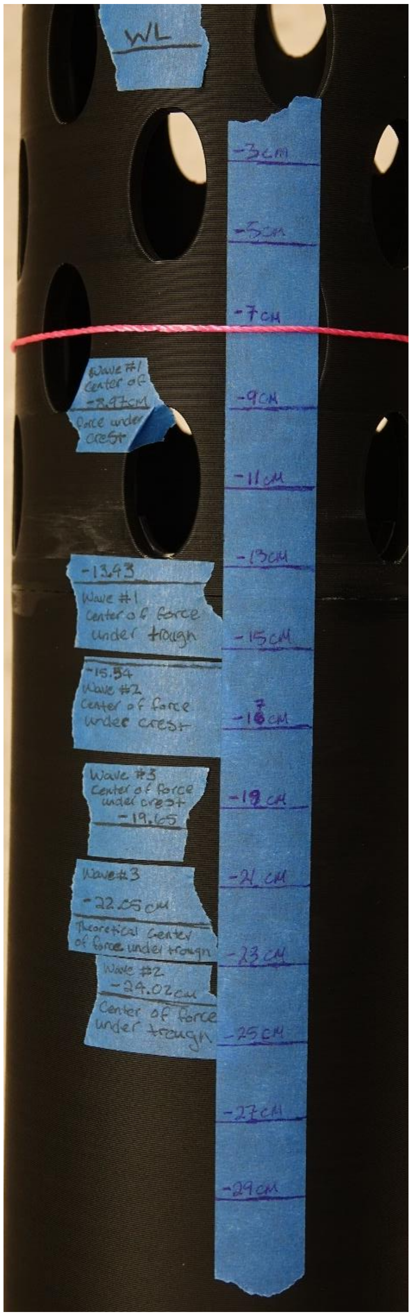

Figure 17: Calibration points and center of force under the crest and trough of test waves #1, #2, and #3 shown on Perforation #2

The calibration procedure was conducted for each of the points shown above in Figure 17 and then the calibration coefficients for each point were plotted against the distance beneath the mean water level. This allows for a line of best fit to be fitted as shown in Figure 18 below.

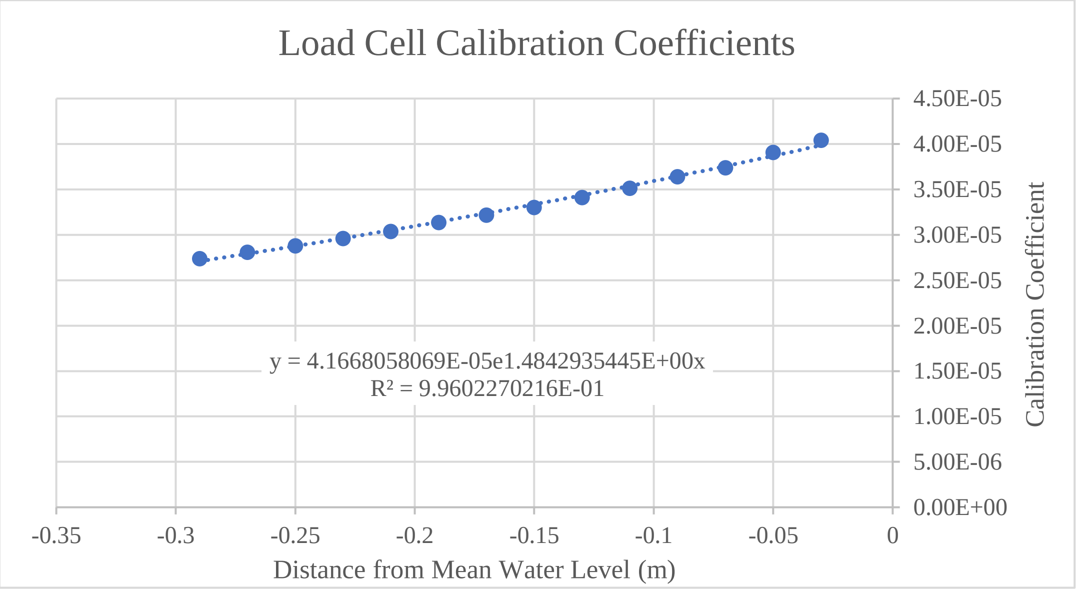

Figure 18: Multipoint Load Cell Calibration Coefficients with Line of Best Fit

The center of force for each wave is determined by taking the wave parameters from the capacitance wave gauges for each wave as it passes the monopiles. The wave parameters are then used to determine the center of force given a time under the wave. The center of force is then plugged into the line of best fit equation for the calibration coefficients, Figure 18.

The wave tank was set up with the monopile attached to the load cell and positioned in the center of the tank. Sonic wave gauges were placed at five locations, the first was 1 m in front of the monopile the other four were placed at 90-degree offsets around the monopile at 8 cm from the centerline of the monopile, Figure 19 and Figure 20.

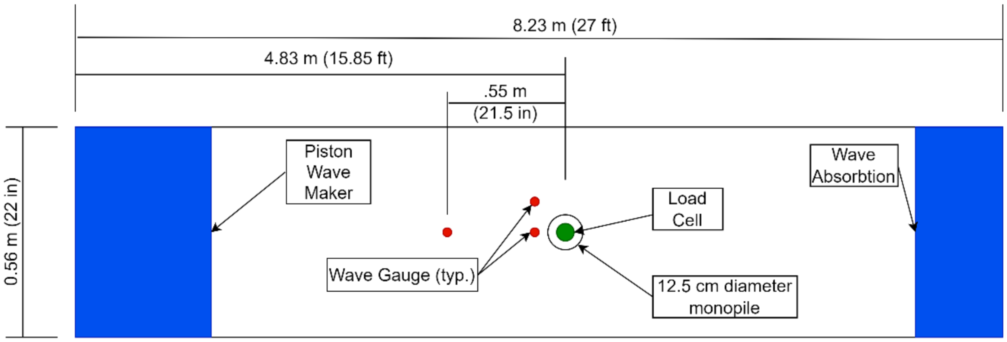

Figure 19: Top View of Wave Tank Experimental Setup

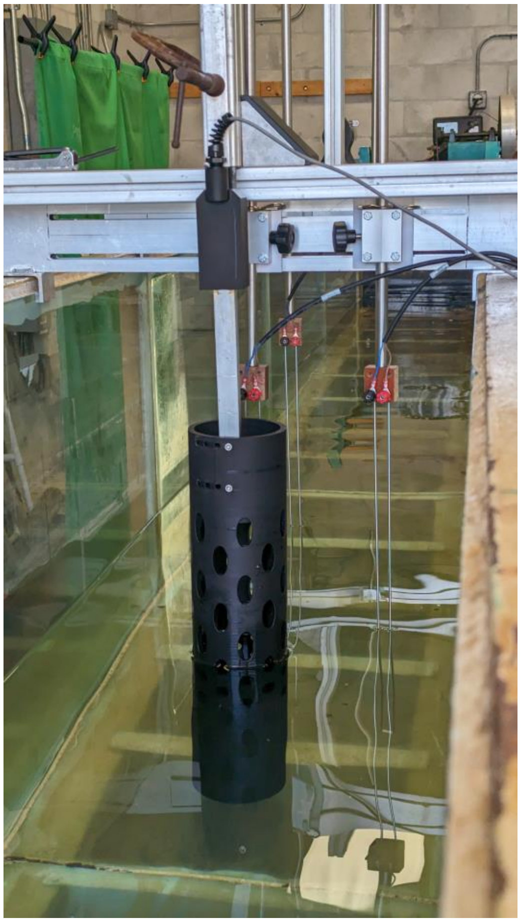

Figure 20: Perforation #2 setup for test wave #2 with capacitance wave gauges

Capacitance wave gauges from Edinburgh Designs, as seen in Figure 21, are being chosen to allow for higher sampling rates to match or exceed the Nyquist frequency or the minimum frequency required to sample the wave without aliasing (Landau, 1967). As the smallest period to be sampled is 0.53 seconds which makes the minimum sampling rate 4 hz. The maximum allowable sampling frequency for the wave probes is 128 hz (Wave Gauges, 2016). Post processing was conducted using MATLAB and a zero-down and up crossing function to verify significant waves heights.

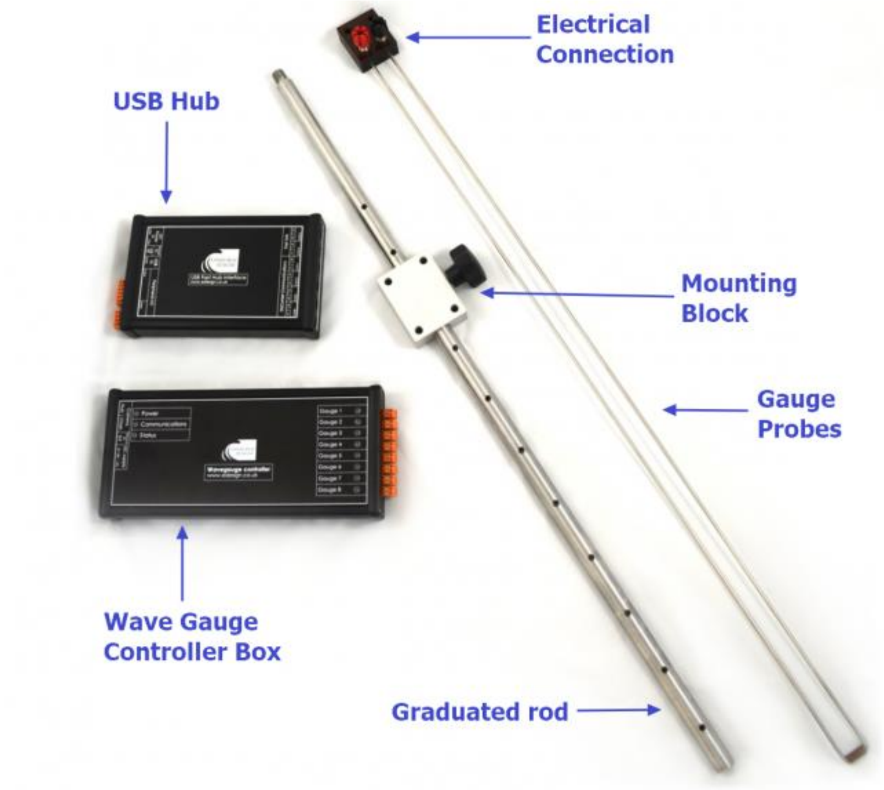

Figure 21: Edinburgh Designs Wave Gauge System (Wave Gauges, 2016)

The physical models used were 3D printed in PLA (polylactic acid), Figure 22, on a Prusa-XL printer from STL (Stereolithography) models generated in Autodesk Fusion 360®. The bed size of the Prusa XL is 14” cubic which allows for large print sizes but still required multiple sections to be printed to form the monopiles. To limit issues due to movement between sections the bottom sections of the monopiles were attached using superglue. The top section was left as a friction fit to allow for editing of the connection to the load cell. As the top section is a friction fit each model setup was subjected to an initial run of a given test wave without recording data. This ensured that if any shifting were to occur in the friction fit it would not impact recorded data.

Figure 22: 3D printed physical models. Pictured from left to right: reference, perforation #1, preforation #2 with connector piece to load cell, perforation #3

CFD Simulations

CFD simulations are conducted with an educational license for Flow-3D® HYRDO which allows for large amplitude non-linear waves to be modeled over coastal structures such as piers and monopiles (FlowScience inc., 2018). The CFD analysis run in Flow-3D® HYDRO will use an imported STL model of the structure from Autodesk Fusion 360®. The selected monopile diameter is 10m with a depth ranging from 33m to 38m; these dimensions match the sizing used by Andersen, et al. (2020) and Ploeg (2021). Scaled simulations were used at a 1:80 scaling to limit required computational power and required mesh sizes. The scaled simulations were run with the geometries, wave characteristics, and pile rotations as explained Table 5 and Table 6 in the Experimental Design section above.

CFD Mesh

The CFD analysis model will require a mesh to be used for calculations. The initial mesh sizing was the coarsest possible to verify model was able to run. Then a mesh sensitivity analysis was conducted to determine the best combination of accuracy while limiting the total number of cells and therefore overall runtime. The mesh sensitivity analysis included sizes from 0.08 to 0.005 to determine where the solution converged for the scaled models.

Each of the analysis models included a secondary mesh surrounding the monopile to resolve the geometry through the FLOW-3D® HYDRO FAVOR™ System. The FAVOR™ or Fractional Area Volume Obstacle Representation is used by FLOW-3D® HYDRO to embed a geometry into the mesh. The geometry is approximated as a plane calculated by the volume of surrounding mesh blocks (Flow Science, Inc., 2018).

As such the minimum mesh size to resolve the scaled geometry is less than the thickness of the scale model which is 0.75 cm. 0.5 cm was used for the mesh to account for the curvature of the model in relation to the cartesian mesh. Variation of the mesh sizes leads to large changes in the total number of cells and therefore the overall runtime, these values can be seen in Table 7 below. The mesh sensitivity testing was conducted on a computer with an Intel® Core™ i7-4790 CPU (central processing unit), 32 GB (gigabyte) of DD3 ram, 2 GB hard drive, a AMD Radeon ™ R7 250 GPU (graphics processing unit) with 2 GB of dedicated ram.

Table 7: Total Cells and Runtimes for Tested Mesh Sizes

Mesh Size (m)	Total Cell Count	Runtime	Output File Size
0.005	33,552,064	4.5 days	115 GB
0.01	4,543,448	10 hr	15 GB
0.02	880,096	1.5 hr	3 GB
0.04	415,772	45 min	915 MB
0.08	357,371	45 min	674 MB

The analysis of the data from each mesh size was handled in MATLAB by determining correlation coefficients between data from one mesh size to another and by visual analysis from graphs. The data points selected for the analysis are pressure force on the monopile in the x & y direction and the pressure from a probe located 2.25 cm in front of the monopile and 18.75 cm beneath the water surface. The correlation coefficients can be seen in Table 8 below and the associated graphs for the 5 second period between 8 and 13 seconds can be seen in Figure 23.

Table 8: Correlation Coefficients for Comparison of Global Mesh Sizes

	Correlation Coefficients			
Compared Mesh Sizes (m)	Pressure Force - Total	Pressure Force - X	Pressure Force - Y	Pressure at Probe
0.005 to 0.01	0.9985	0.9719	0.9988	0.9993
0.01 to 0.02	0.9946	0.8937	0.9956	0.9976
0.02 to 0.04	0.8988	0.3758	0.9038	0.9774
0.04 to 0.08	0.4811	0.2097	0.645	0.9636

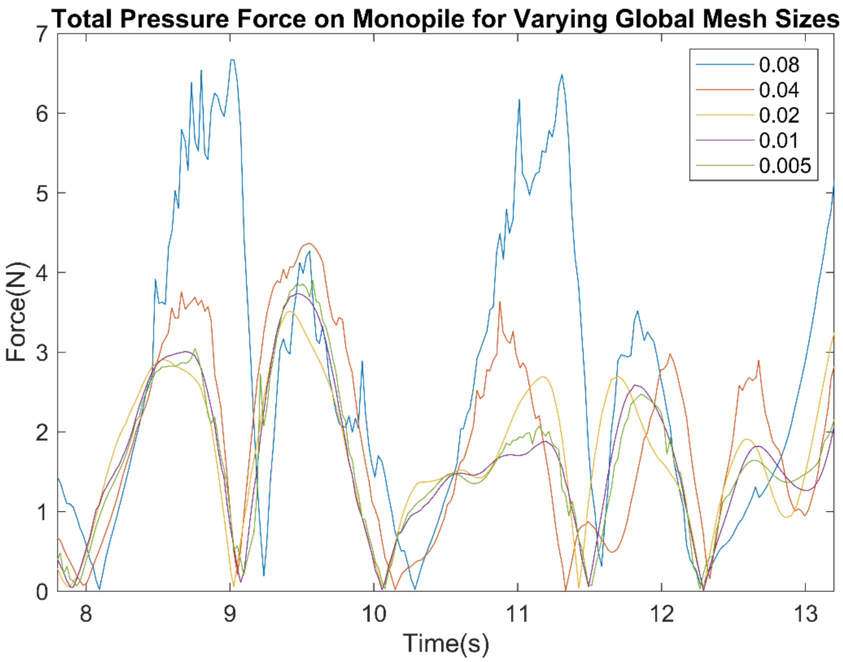

Figure 23: Total pressure force on monopile for varying global mesh sizes

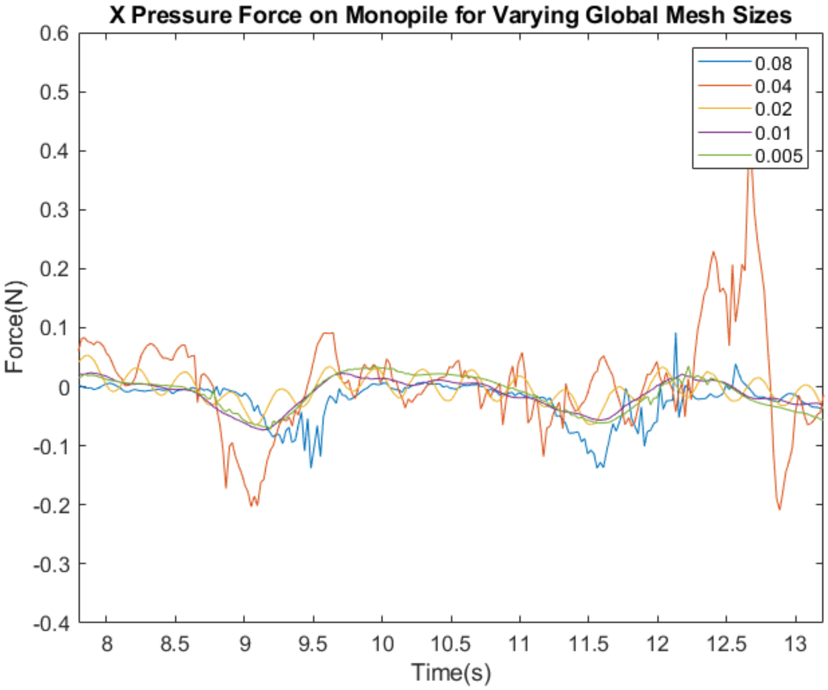

Figure 24: X pressure force on monopile for varying global mesh sizes

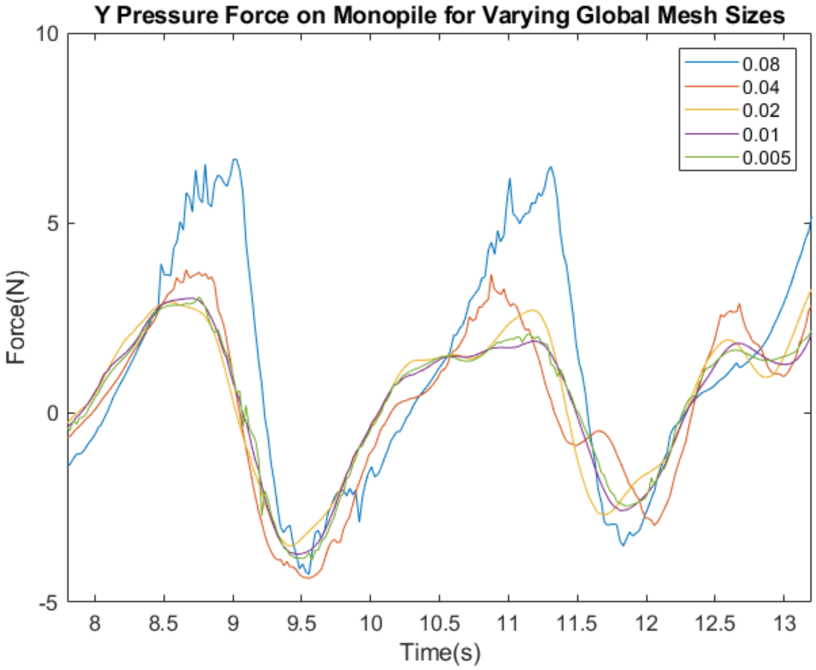

Figure 25: Y pressure force on monopile for varying global mesh sizes

The correlation coefficients and graphs show that the best correlation for x and y is between global mesh sizes of 0.005 and 0.01. However as 0.005 is so computationally expensive, taking over 4 days to complete and generating a file of 115 GB, 0.01 was used as the mesh size for scaled models. It should be noted that after the sensitivity analysis was performed on the reference monopile the local mesh size had to be reduced to 0.0025 m around the monopile itself to allow for the FAVOR™ system to resolve the perforations. This adjustment increased the total cell count for the simulation to 6,989,528 and increased the model runtime to just over 1 day.

In addition to the mesh, boundary conditions for the CFD model must be set and can be found in Table 9 below.

Table 9: Boundary Conditions for CFD Model

Boundary	Condition
X Minimum	Symmetry
X Maximum	Symmetry
Y Minimum	Wave Inflow – Stokes and Cnoidal waves
Y Maximum	Wave Outflow with Wave Absorption
Z Minimum	Symmetry
Z Maximum	Pressure

The y minimum boundary condition will vary between Stokes and Cnoidal waves and Fenton's (5th Order Stokes) waves as determined by Figure 26 below. The figure shows where differing wave theories apply based on the wave height, period and depth of water. If the applicable wave theory based on the graph below was above 2nd order stokes, Fenton's 5th order was used to ensure accuracy.

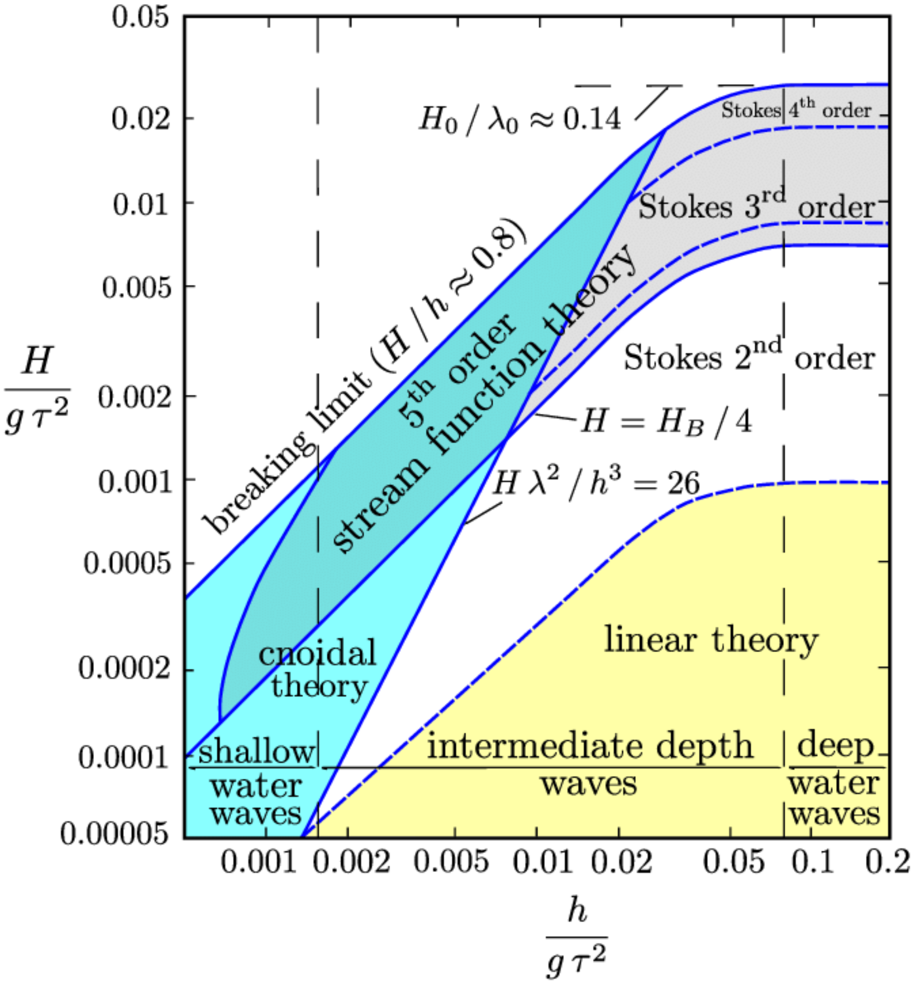

Figure 26: Applicable ranges of numerical wave theories (L.H. Holthuijsen, 2007)

Chapter 3

Results

CFD Simulations

The forces for each wave showed greater reductions as the perforation size increased and the greatest force reductions were seen for test wave #1 from Table 6 which had the lowest KC, Figure 27 to Figure 29. A line of best fit was applied to the data by minimizing the root mean square error (RMSE) of the function below by changing variables a and b.

$$F_{fit} = a * \tanh(b * KC) \tag{16}$$

The CFD simulation results were compared to previous research by determining R^2 values. All R^2 values shown here-in are comparisons between lines of best fit. The R^2 values range from 0.7877 to 0.9716 showing a general agreement to previous research for the force reduction vs. KC number.

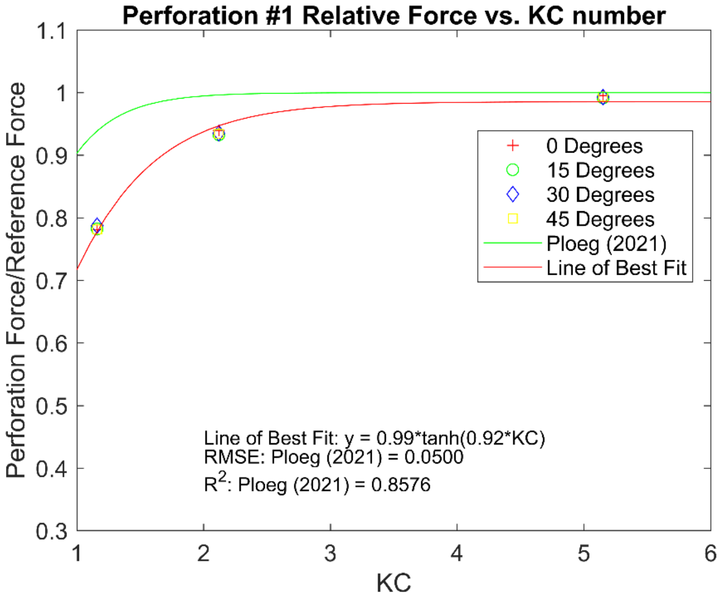

Figure 27: Relative force comparison of perforation #1 from CFD results vs. KC number with generated line of best fit (red) and line of best fit from Ploeg (2021) (green)

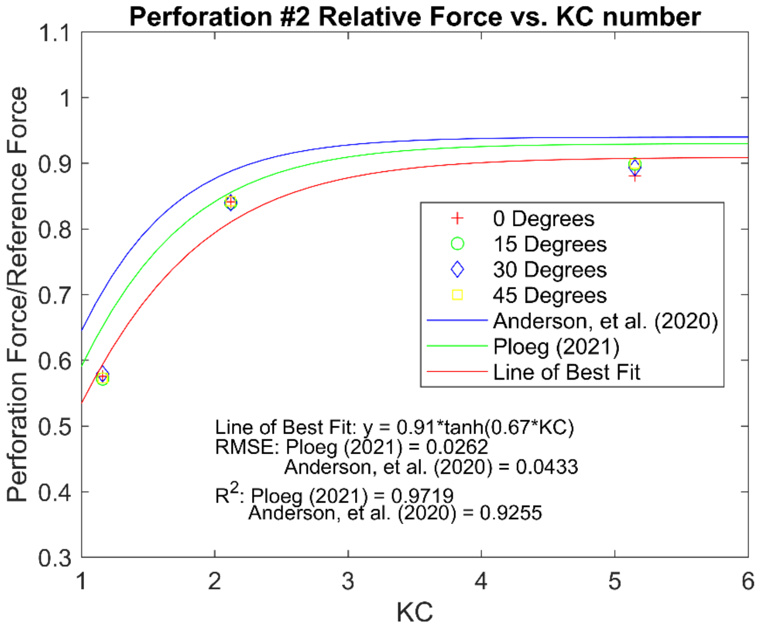

Figure 28: Relative force comparison of perforation #2 from CFD results vs. KC number with generated line of best fit (red) and lines of best fit from Andersen, et al. (2020) (blue) and Ploeg (2021) (green)

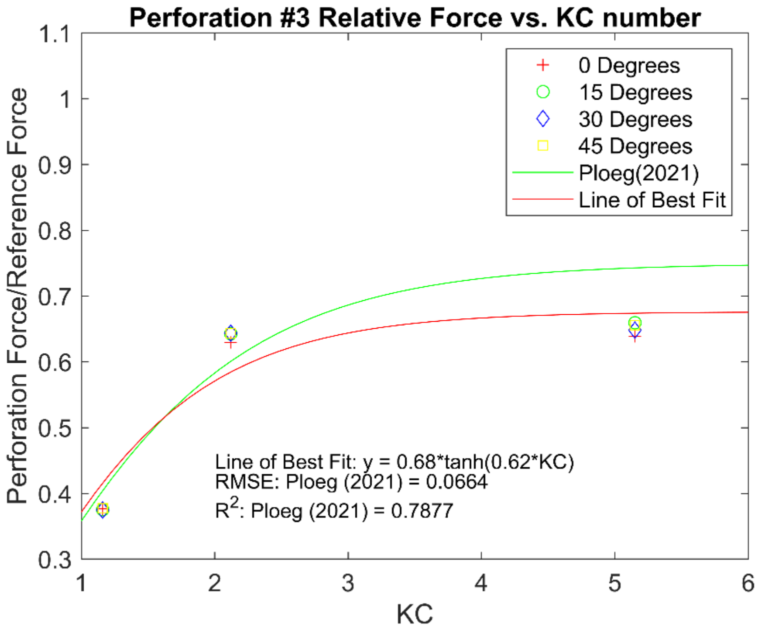

Figure 29: Relative force comparison of perforation #3 from CFD results vs. KC number with generated line of best fit and line of best fit (red) from Ploeg (2021) (green)

The averaged forces from each perforation and each wave show greater force reductions at larger perforation sizes and at waves with lower KC numbers, Table 10. While the recorded force reductions from CFD follow the general fit of previous research a direct force comparison with Andersen, et al. (2020) shows a large difference between results for test wave #2, Table 10 and Table 11. This difference is attributed to a difference in the wave height impacting the monopile. Andersen, et al. (2020) recorded a wave height of 9.88m (0.1235m scaled) impacting the reference monopile and a 9.99m (0.12485m scaled) wave impacting the perforated monopile which has the same geometry as perforation #2 (Table 2). The recorded wave heights with the model in place from Andersen, et al. (2020) can be found in

Table 10: Peak forces from CFD simulations for test waves in Table 6

CFD Simulation Peak Forces			
Monopile	Wave 1	Wave 2	Wave 3
Reference	6.137 N	13.468 N	3.270 N
Perforation 1	4.806 N	13.372 N	3.059 N
Perforation 2	3.529 N	11.826 N	2.749 N
Perforation 3	2.309 N	9.525 N	2.094 N
Wave Height	4.75 cm	13.5 cm	4.25 cm

Table 11: Peak forces from Andersen, et al. (2020) for test waves 1, 2, and 3

Anderson et al. (2020) Peak Forces				
Monopile	Variable	Wave 1	Wave 2	Wave 3
Reference	Force	6.222 N	10.930 N	3.148 N
	Height	3.763 cm	12.350 cm	3.525 cm
Perforation 2	Force	3.969 N	10.076 N	2.782 N
	Height	3.975 cm	12.488 cm	3.563 cm
Andersen et al. (2020) Peak Forces				
Monopile	Wave 1	Wave 2	Wave 3	
Reference	6.222 N	10.930 N	3.148 N	
Perforation 2	3.969 N	10.076 N	2.782 N	

Due to the difference in wave heights, Table 10 and Table 11, a direct force comparison between the CFD testing and Anderson, et al. (2020) could not be conducted. Therefore, an additional CFD simulation was run to conduct a comparison of forces. Test wave #2 was selected to run an additional CFD simulation on the reference monopile as test wave #2 showed the largest difference in wave height between the original testing and previous research. The additional CFD result had a peak force within 3.4% of that from Andersen, et al. (2020), Table 12.

Table 12: CFD results for wave parameters matching Andersen, et al. (2020) and % force difference from Andersen, et al.(2020)

CFD Results for Andersen, et al.(2020) Wave Parameters				
Monopile	Force (N)	Wave Height (m)	Wave Period(s)	% Difference
Reference	10.557	12.34	1.683	3.4126%

The observed wave parameters in the wave tank testing also varied greatly from the initial test waves. Additional CFD simulations were run with the observed wave parameters from the wave tank to allow for a force comparison to be conducted, Table 13. The additional simulations overestimate the force reduction for test waves #1 and #2 and underestimate the force reduction for test wave #3 when compared with the previous CFD results, Figure 30 to Figure 32. This force reduction pattern is consistent for each of the perforations. Correlation values between the new CFD results and the previously generated line of best fit range from $R^2 = 0.8621$ to 0.9614.

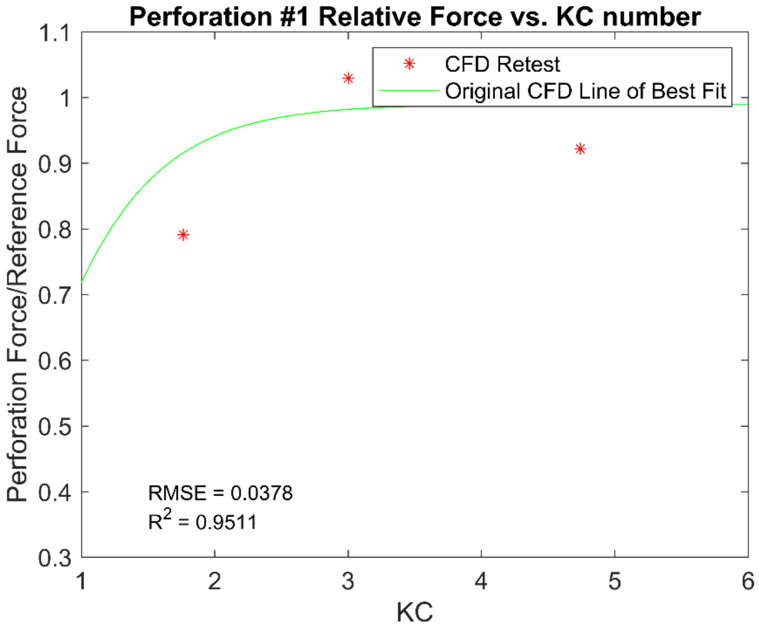

Figure 30: Comparison of force reduction from CFD analysis based on observed wave parameters from wave tank for perforation #1 with line of best fit from orignial CFD simulations (green)

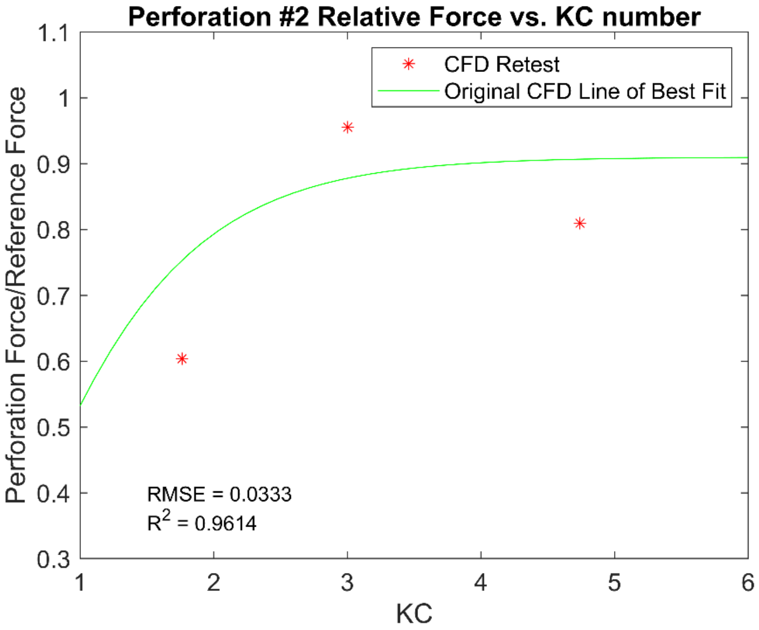

Figure 31: Comparison of force reduction from CFD analysis based on observed wave parameters from wave tank for perforation #2 with line of best fit from orignial CFD simulations (green)

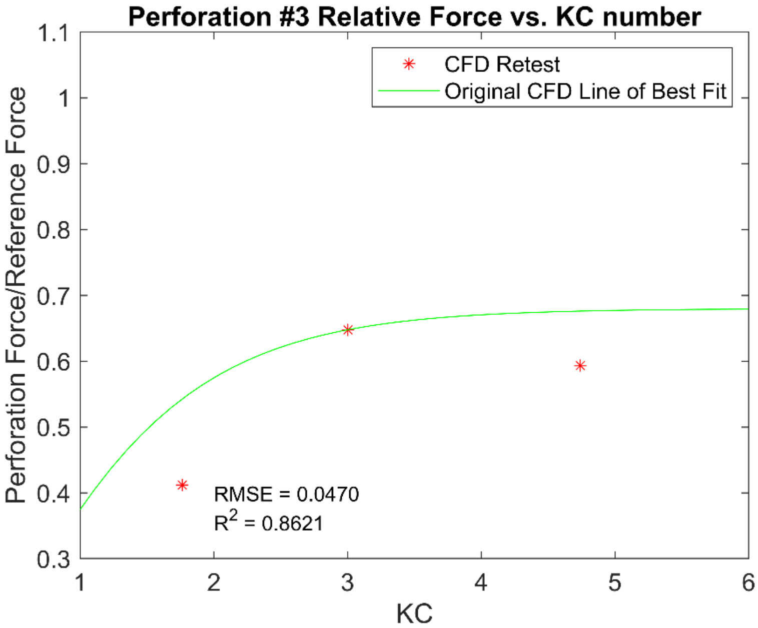

Figure 32: Comparison of force reduction from CFD analysis based on observed wave parameters from wave tank for perforation #1 with line of best fit from orignial CFD Simulations (green)

Wave Tank Testing

Raw data from the wave tank testing had to be windowed to prevent analysis of waves affected by reflection. Sloped rocks were placed at the end of the wave tank to minimize reflection. However, both test wave #2 and test wave #3 both resulted in observable reflections, Figure 33 & Figure 34.

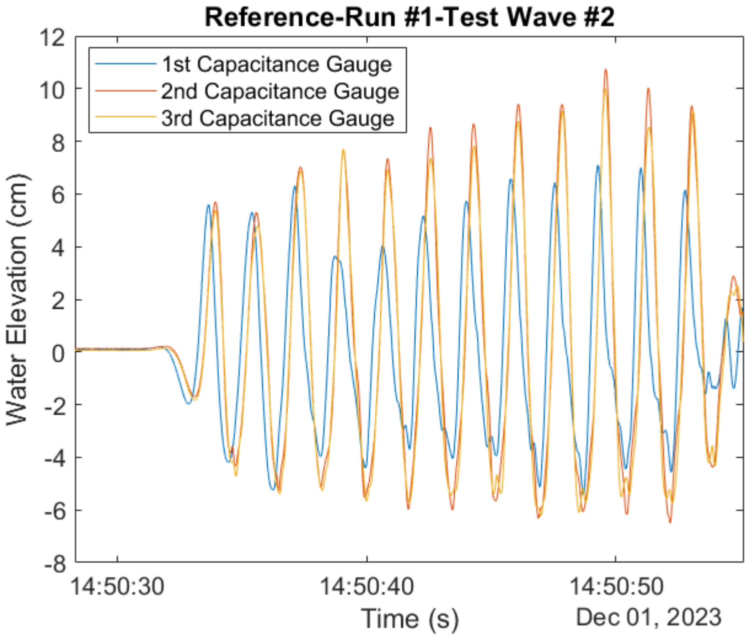

Figure 33: Wave elevation history for run #1 of test wave #2 on the reference monopile

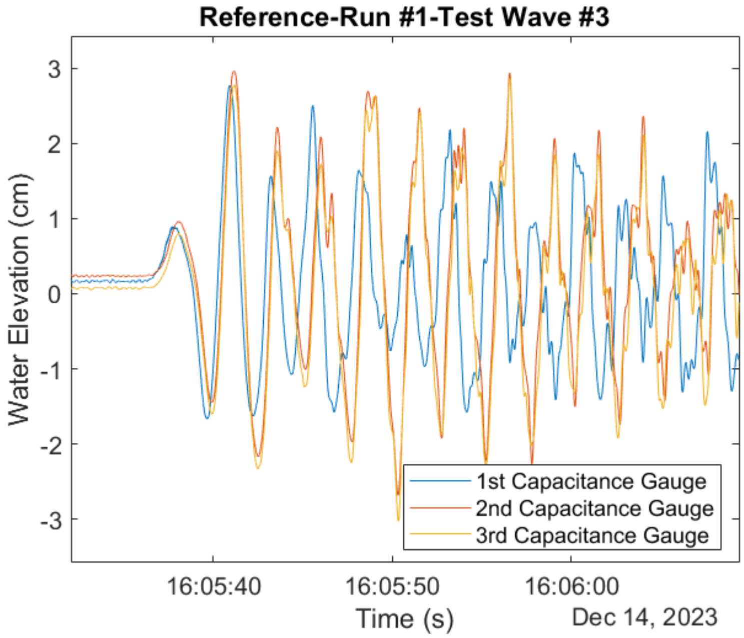

Figure 34: Wave elevation history for run #1 of test wave #3 on the reference monopile

The averaged observed wave parameters (Table 13) were used to conservatively determine the time at which a fully reflected wave would reach the monopile.

This was done by determining the time it would take the observed wave to travel past the monopile to the end of the wave tank and back. The travel time was then added to the point at which the first wave action was seen by wave gauge #3. The reflected waves take 3.67s and 3.45s to reach the monopile after initial wave action was seen at wave gauge #3 for test waves #2 and #3 respectively, Table 13.

Table 13: Averaged observed wave parameters during wave tank testing

Wave Tank Wave Parameters			
	Wave 1	Wave 2	Wave 3
Height (m)	0.05815	0.10306	0.050279
Period (s)	0.85667	1.6703	2.4653
Length (m)	1.1284	3.0947	4.8584
Reflection Time (s)	5.1625	3.6702	3.4505
KC Number	1.7647	4.7396	3.0017

The end of the second wave was on average 5.447s and 7.268s behind the initial wave action for test waves #2 and #3 respectively. As the end of the second wave occurs after the reflected wave reaches the wave gauge only the first wave of each test run for test waves #2 and #3 could be used for analysis. The averaged observed wave parameters in Table 13 above reflect the windowing for the first wave of test waves #2 and #3.

The relative force reductions from the wave tank testing of test waves #1 and #2 for perforations 1, 2, and 3 are greater than those presented by previous research and the generated line of best fit for the initial CFD simulations. While the force reduction from test wave #3 undercuts the CFD model and previous research lines of best fit, Figure 35 to Figure 37. The resulting line of best fit from the wave tank results have R^2 values of 0.9683 or above with the initial CFD results and an R^2 value of 0.7062 or above with previous research.

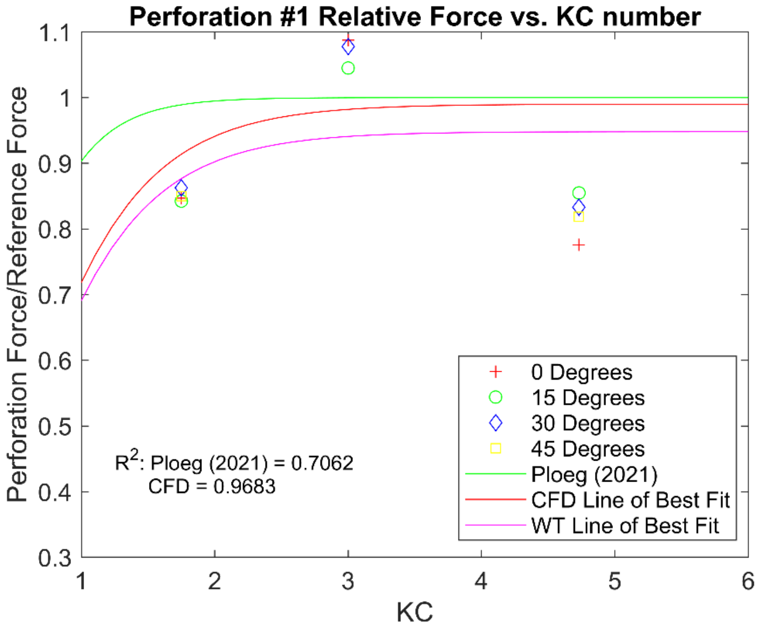

Figure 35: Relative force comparison of perforation #1 from wave tank results vs. KC number with generated line of best fit (magenta), and lines of best fit from CFD (red) and Ploeg (2021) (green)

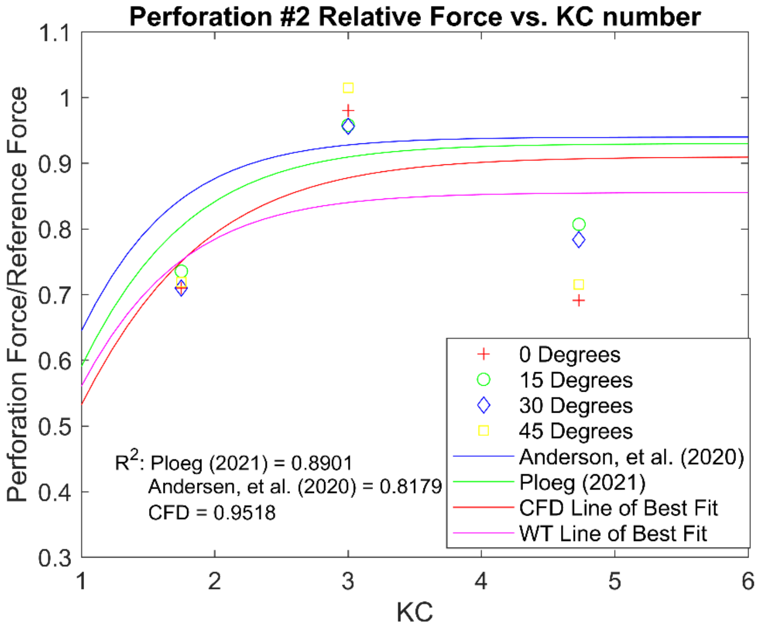

Figure 36: Relative force comparison of perforation #2 from wave tank results vs. KC number with generated line of best fit (magenta), and lines of best fit from CFD (red), Andersen, et al.(2020) (blue) and Ploeg (2021) (green)

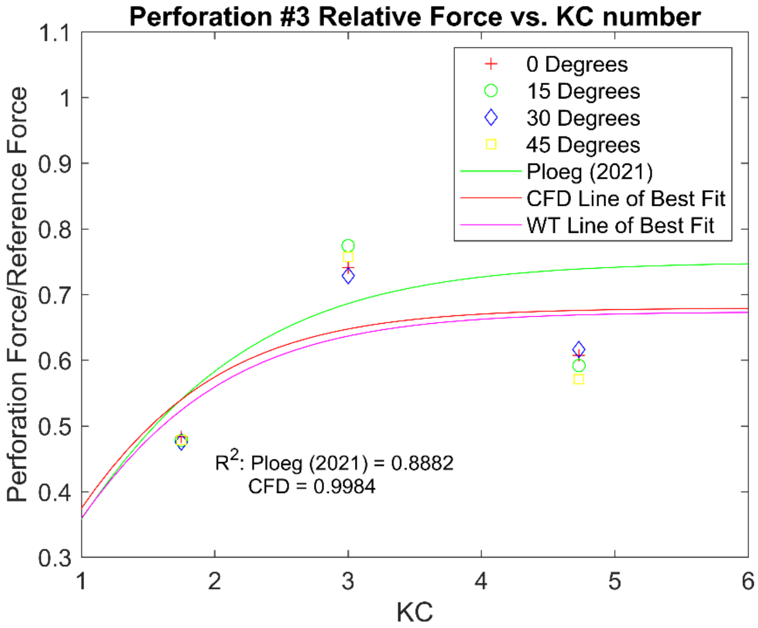

Figure 37: Relative force comparison of perforation #3 from wave tank results vs. KC number with generated line of best fit (magenta) and lines of best fit from CFD (red) and Ploeg (2021) (green)

After the initial set of wave tank testing additional runs were conducted for the reference monopile using test wave #2 to allow for a direct comparison of forces with previous research. The wave height for these additional test runs were modified to match the wave heights observed by Andersen, et al. (2020). The resultant force of the reference monopile is 5.9% different than that recorded by Andersen, et al. (2020), Table 14.

Table 14: Wave tank peak forces for test waves with wave heights matching the observed model heights from Andersen, et al. (2020) for the reference monopile

Wave Tank Peak Forces – Andersen, et al. (2020) Observed Parameters			
Monopile	Force (N)	Wave Height (m)	Wave Period (s)
Reference	10.278	0.123645	1.586

To allow for force comparison of the wave tank testing with the CFD simulations additional CFD simulations and numerical analysis were run using the wave parameters in Table 13. The results of the additional CFD simulations can be seen in the CFD Simulation section above. When compared with the wave tank results correlation values of 0.8985 to 0.9260 are observed, Figure 38 to Figure 40. For each wave in the wave tank variations of +/- 1N can be observed as seen in the direct comparison of the observed forces from the wave tank and from the CFD Simulation in Table 15 and Table 16.

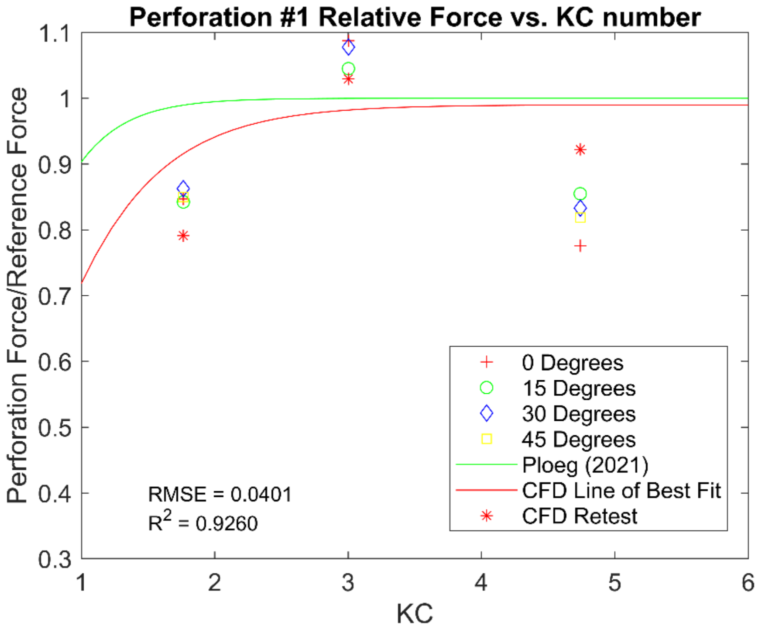

Figure 38: Comparison of force reduction from CFD analysis based on observed wave parameters from wave tank for perforation #1 with respective wave tank results and lines of best fit from Ploeg (2021) (green) and CFD (red)

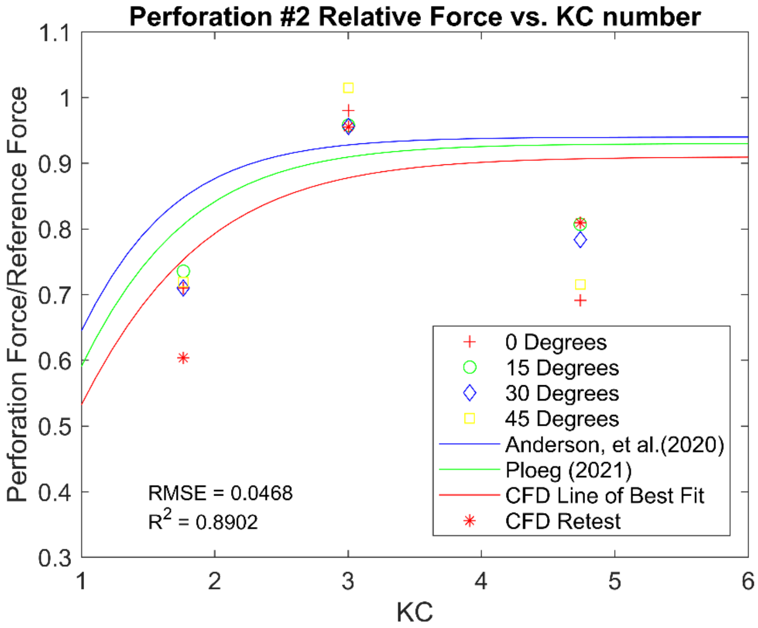

Figure 39: Comparison of force reduction from CFD analysis based on observed wave parameters from wave tank for perforation #2 with respective wave tank results and lines of best fit from Andersen, et al. (2020) (blue), Ploeg (2021) (green) and CFD (red)

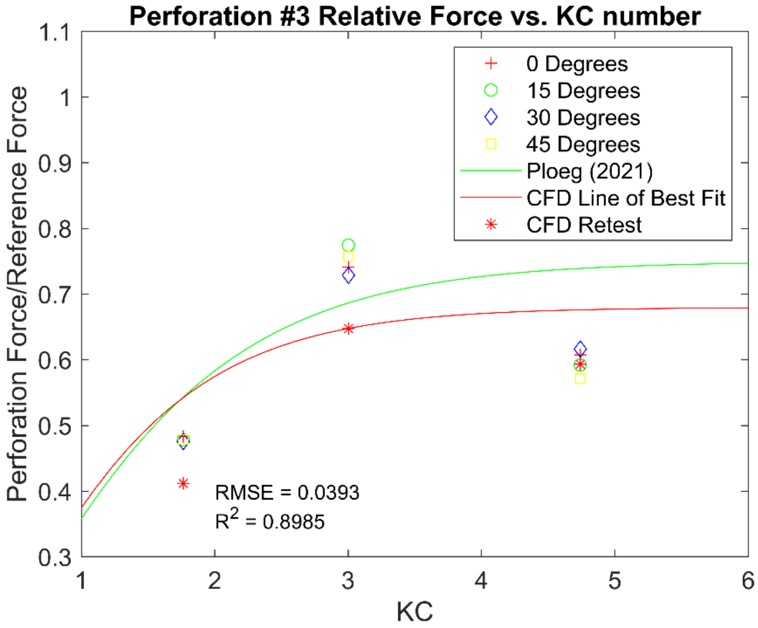

Figure 40: Comparison of force reduction from CFD analysis based on observed wave parameters from wave tank for perforation #3 with respective wave tank results and lines of best fit from Ploeg (2021) (green) and CFD (red)

Table 15: Wave Tank Peak Forces

Wave Tank Peak Forces			
Monopile	Wave 1	Wave 2	Wave 3
Reference	7.904 N	9.940 N	2.825 N
Perforation 1	6.723 N	8.564 N	3.304 N
Perforation 2	5.458 N	7.454 N	2.706 N
Perforation 3	3.786 N	5.332 N	2.121 N

Table 16: Peak forces from CFD Simulations using observed wave parameters from wave tank tests

CFD Peak Forces for Wave Tank Parameters			
Monopile	Wave 1	Wave 2	Wave 3
Reference	7.183 N	10.166 N	3.855 N
Perforation 1	5.684 N	9.375 N	3.969 N
Perforation 2	4.337 N	8.230 N	3.368 N
Perforation 3	2.961 N	6.034 N	2.497 N

While the force between the additional CFD simulations and the original wave tank testing varies, the resultant reductions in force are within ±10% between the physical models and simulations, Table 17. The CFD and wave tank wave parameters shown in Appendix B are close with variations of 1.5 cm or less in wave height.

Table 17: Comparison of forces and percent force reduction between wave tank results and CFD simulations with wave parameters observed from wave tank physical model testing.

	Monopile	Wave Tank Results	CFD Results 2	Percent Force Reduction		Difference in Force Reduction
		Force (N)	Force (N)			
Wave #1	Reference	7.9039	7.1827	15%	21%	-6%
	Perforation #1	6.7226	5.6838			
	Perforation #2	5.4575	4.3367	31%	40%	-9%
	Perforation #3	3.7857	2.9607	52%	59%	-7%
	Reference	9.9396	10.166	18%	8%	10%
	Perforation #1	8.1572	9.3752			

Wave #2	Perforation #2	7.4541	8.2302	25%	19%	6%
	Perforation #3	5.9332	6.0344	40%	41%	0%
Wave #3	Reference	2.8253	3.8550	-9%	-3%	-6%
	Perforation #1	3.0893	3.9687			
	Perforation #2	2.7062	3.3683	4%	13%	-8%
	Perforation #3	2.1205	2.4969	25%	35%	-10%

Rotation of Monopiles

The perforated monopiles were tested at 0, 15, 30, and 45 degrees of rotation in relation to the on-coming wave. The rotation testing was conducted in both the wave tank and in FLOW-3D® HYDRO simulations. The difference due to rotation is under 2% of average force in the CFD results and under 7% of the average force in the physical modeling results. The average peak forces of each rotation and the percent difference from the total averaged force for that perforation in each test wave can be seen in Table 18 for the CFD results and Table 19 for the wave tank results.

Table 18: CFD peak force values and percent different from average force for each perforation at each rotation for each wave

Rotation Analysis of CFD Results							
Perforation	Rotation	Wave #1		Wave #2		Wave #3	
		Peak Force (N)	% Difference from Average	Peak Force (N)	% Difference from Average	Peak Force (N)	% Difference from Average
1	0	4.79	0.00%	13.41	0.00%	3.07	0.00%
	15	4.80	0.15%	13.36	-0.38%	3.05	-0.73%
	30	4.83	0.80%	13.37	-0.25%	3.06	-0.48%
	45	4.80	0.06%	13.38	-0.19%	3.05	-0.58%
2	0	3.53	0.00%	11.87	0.00%	2.75	0.00%
	15	3.51	-0.74%	12.11	2.01%	2.75	-0.21%
	30	3.56	0.60%	12.03	1.37%	2.75	-0.18%
	45	3.52	-0.46%	12.11	2.05%	2.75	0.08%

3	0	2.31	0.00%	8.61	0.00%	2.06	0.00%
	15	2.30	-0.34%	8.88	3.22%	2.10	2.09%
	30	2.30	-0.51%	8.73	1.48%	2.10	2.22%
	45	2.32	0.20%	8.84	2.65%	2.10	2.18%

Table 19: Wave Tank peak force values and percent different from average force for each perforation at each rotation for each wave

Rotation Analysis of Wave Tank Results							
Perforation	Rotation	Wave #1		Wave #2		Wave #3	
		Peak Force (N)	% Difference from Average	Peak Force (N)	% Difference from Average	Peak Force (N)	% Difference from Average
1	0	6.69	0.00%	7.71	0.00%	3.07	0.00%
	15	6.66	-0.53%	8.50	10.17%	2.95	-3.91%
	30	6.82	1.87%	8.28	7.38%	3.04	-0.91%
	45	6.72	0.37%	8.13	5.46%	3.29	6.99%
2	0	5.38	0.00%	7.11	0.00%	2.71	0.00%
	15	5.60	4.08%	7.96	12.01%	2.65	-2.23%
	30	5.39	0.31%	7.59	6.89%	2.65	-2.47%
	45	5.46	1.65%	7.16	0.74%	2.81	3.60%
3	0	3.82	0.00%	6.04	0.00%	2.09	0.00%
	15	3.78	-1.16%	5.89	-2.54%	2.19	4.52%
	30	3.76	-1.59%	6.13	1.47%	2.06	-1.66%
	45	3.79	-0.91%	5.68	-5.93%	2.14	2.20%

The tables show no obviously noticeable correlation between the rotation, perforation size or test waves. The absence of a correlation is easier to view in Figure 41 to Figure 46 which show the % difference from average for each wave.

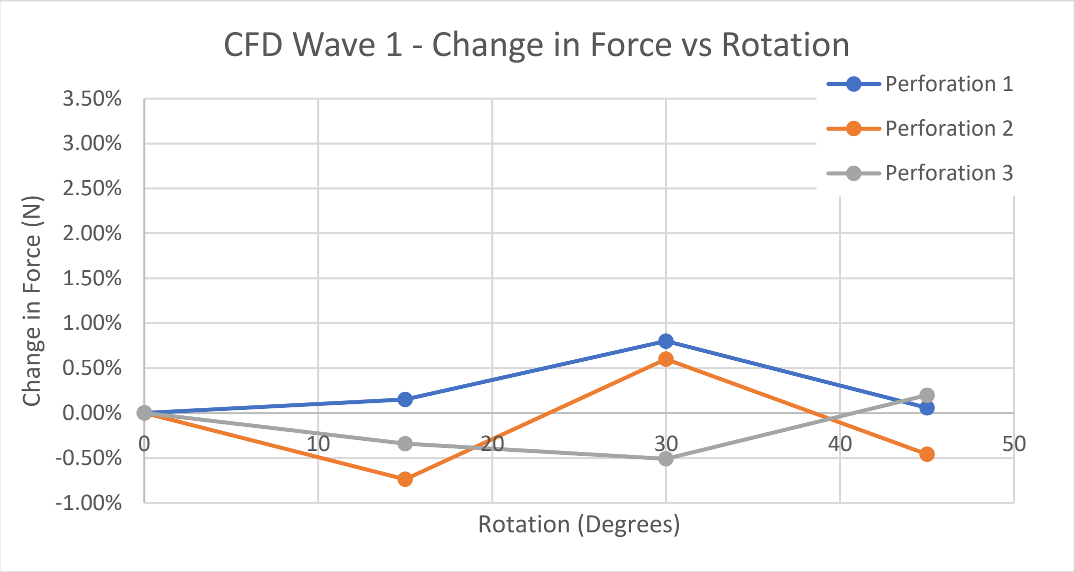

Figure 41: Percent change in force from average for each perforation from CFD test wave #1 plotted against the rotation of the monopile in degrees

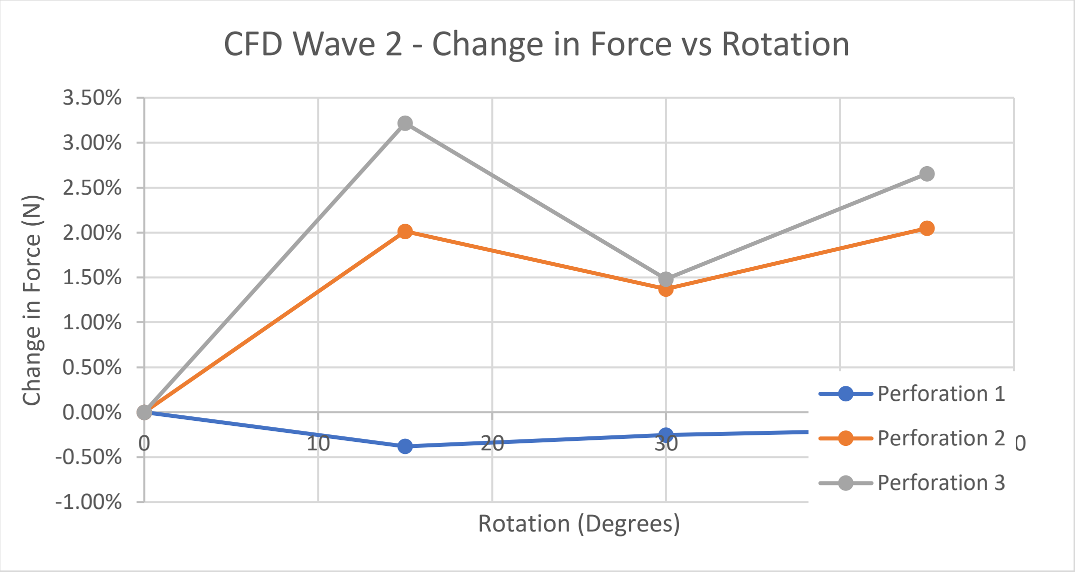

Figure 42: Percent change in force from average for each perforation from CFD test wave #2 plotted against the rotation of the monopile in degrees

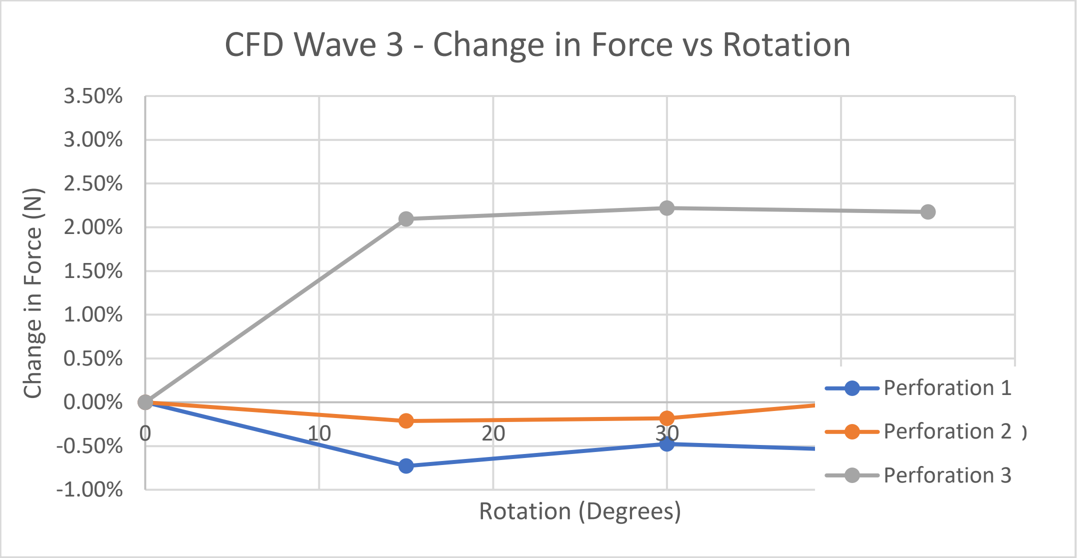

Figure 43: Percent change in force from average for each perforation from CFD test wave #3 plotted against the rotation of the monopile in degrees

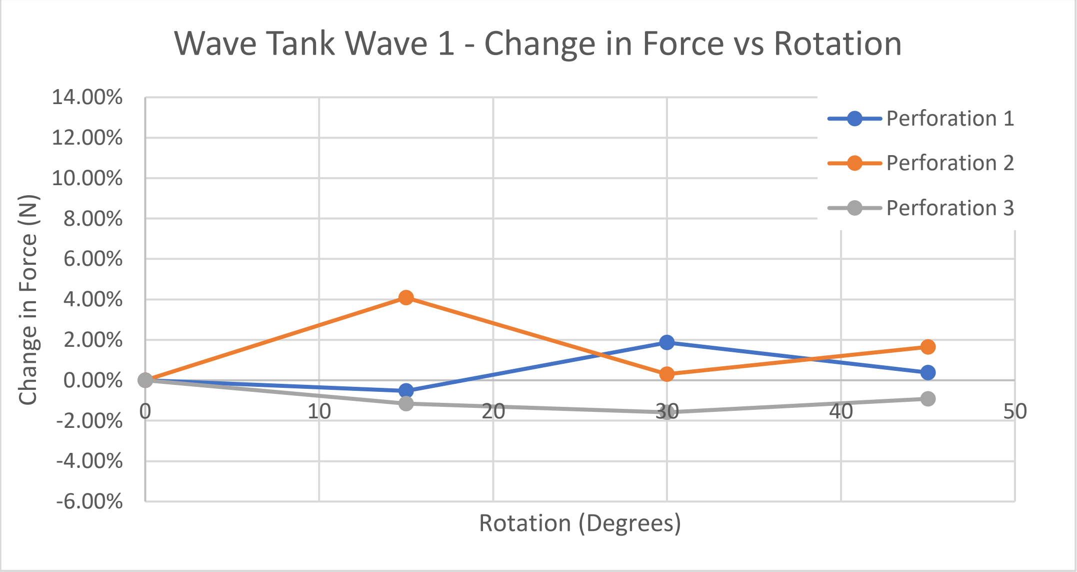

Figure 44: Percent change in force from average for each perforation from wave tank test wave #1 plotted against the rotation of the monopile in degrees

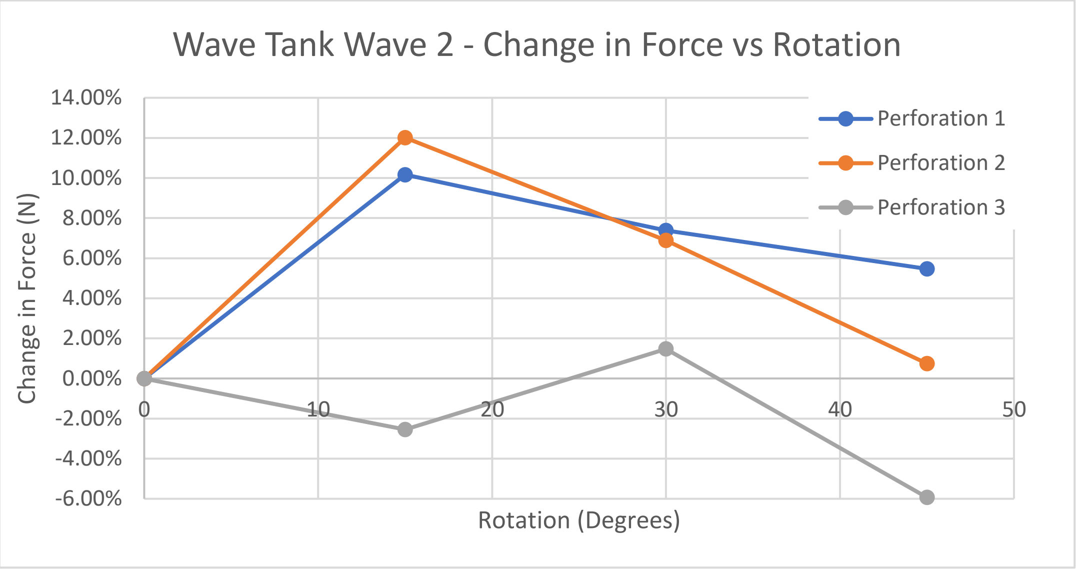

Figure 45: Percent change in force from average for each perforation from wave tank test wave #2 plotted against the rotation of the monopile in degrees

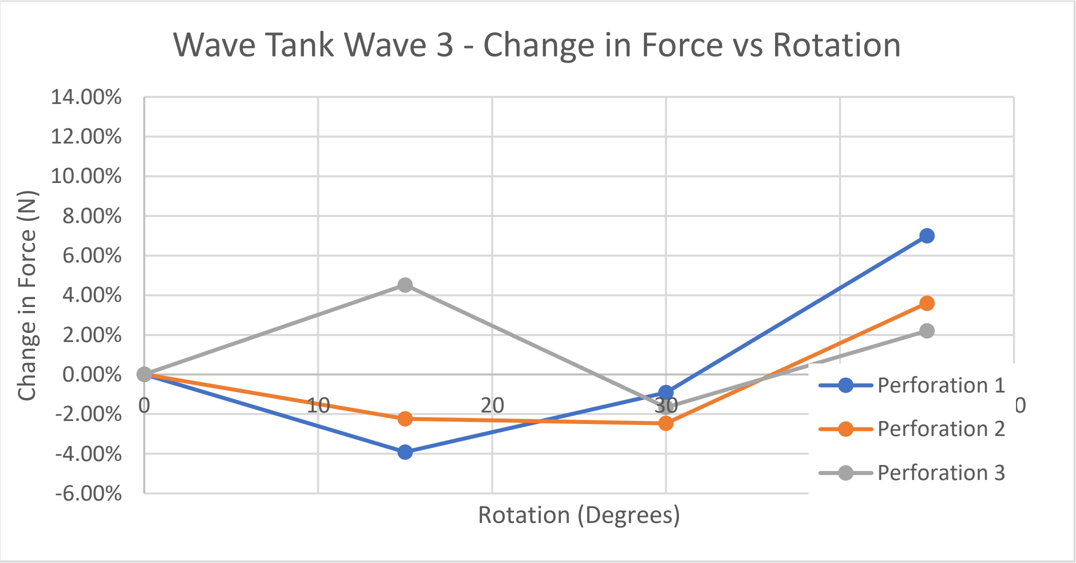

Figure 46: Percent change in force from average for each perforation from wave tank test wave #3 plotted against the rotation of the monopile in degrees

From wave to wave the trends between the individual perforations are not consistent. While the largest changes in forces in the CFD simulations occur for the largest perforation this is not correlated by the wave tank results. The wave tank results show forces for every perforation vary where the largest difference in force can be seen more consistently for perforations 1 and 2. It should be noted that most of the largest % differences can be seen for test wave 2 which has the highest KC number. As such the data was replotted with a graph for each rotation and each graph showing % difference in force vs. KC number of a given wave.

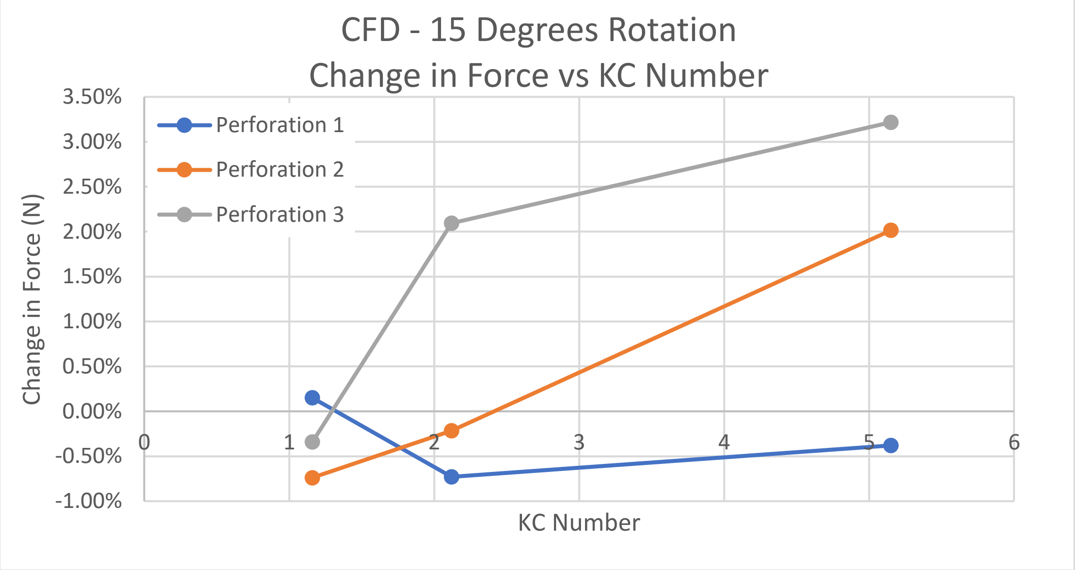

Figure 47: Percent change in CFD peak force from average for each perforation for a rotation of 15 degrees against the KC number of tested waves

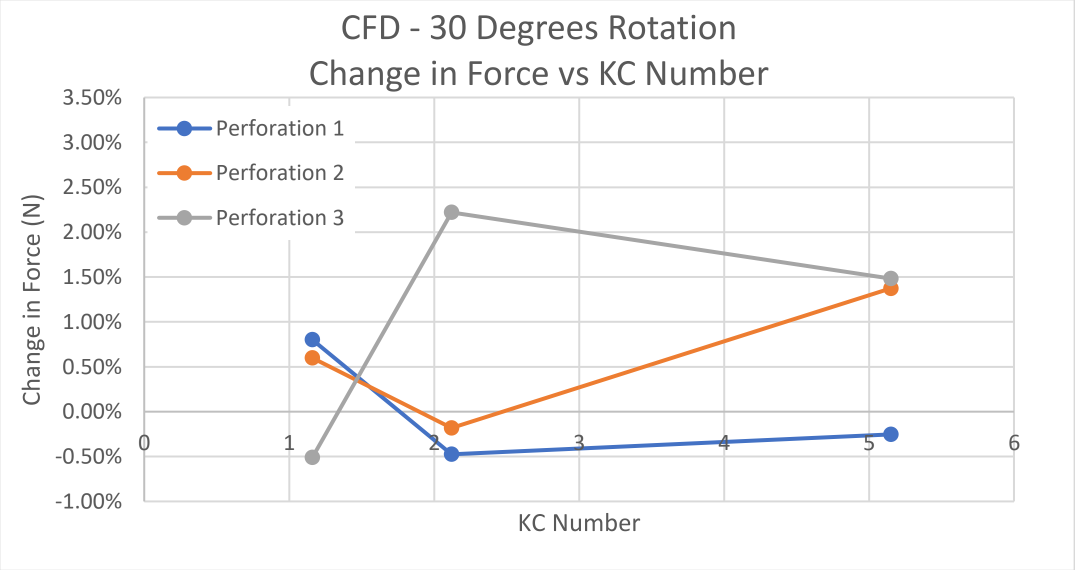

Figure 48: Percent change in CFD peak force from average for each perforation for a rotation of 30 degrees against the KC number of tested waves

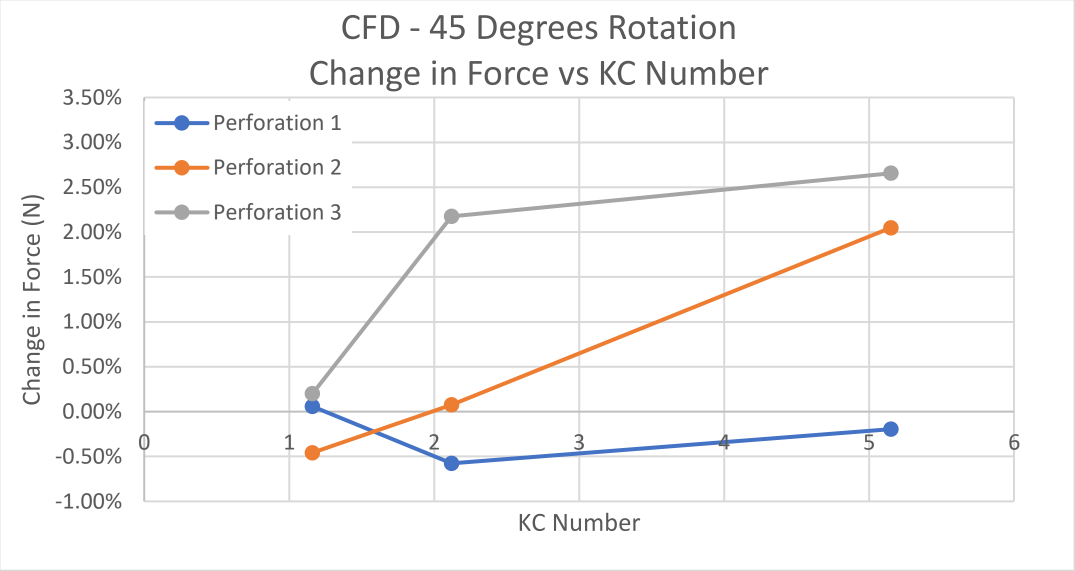

Figure 49: Percent change in CFD peak force from average for each perforation for a rotation of 45 degrees against the KC number of tested waves

Both the 15° and 45° rotations of the CFD analysis show an upwards trend in force in correlation with the KC number and perforation size, Figure 47 and Figure 49. At the 30° rotation, SEQ Figure * ARABIC Figure 48, the correlation is not as clear but the difference from the average tends to be lower for higher KC numbers than the difference shown by the 15° and 30° rotations.

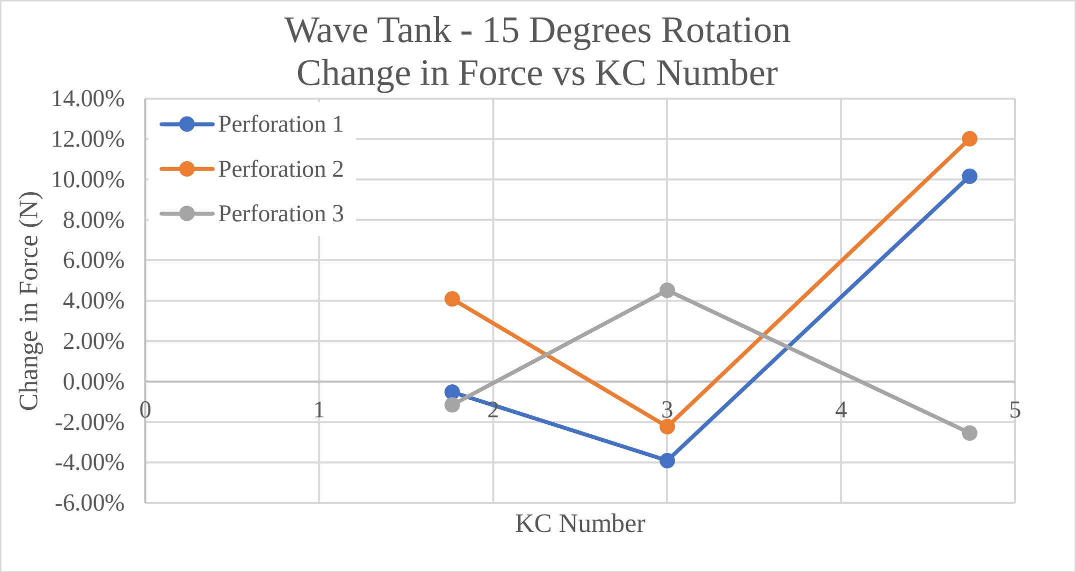

Figure 50: Percent change in wave tank peak force from average for each perforation for a rotation of 15 degrees against the KC number of tested waves

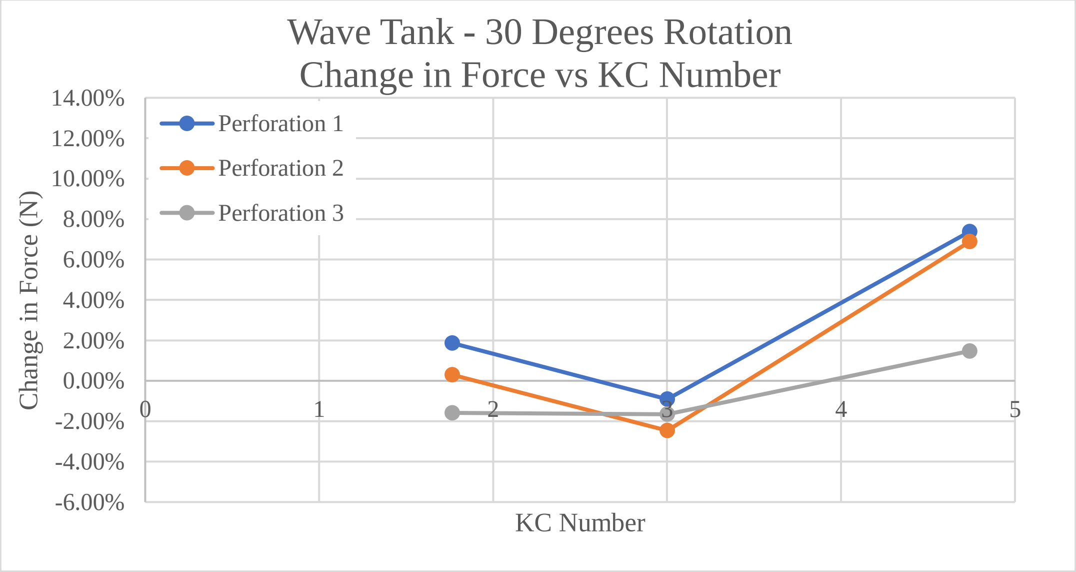

Figure 51: Percent change in wave tank peak force from average for each perforation for a rotation of 30 degrees against the KC number of tested waves

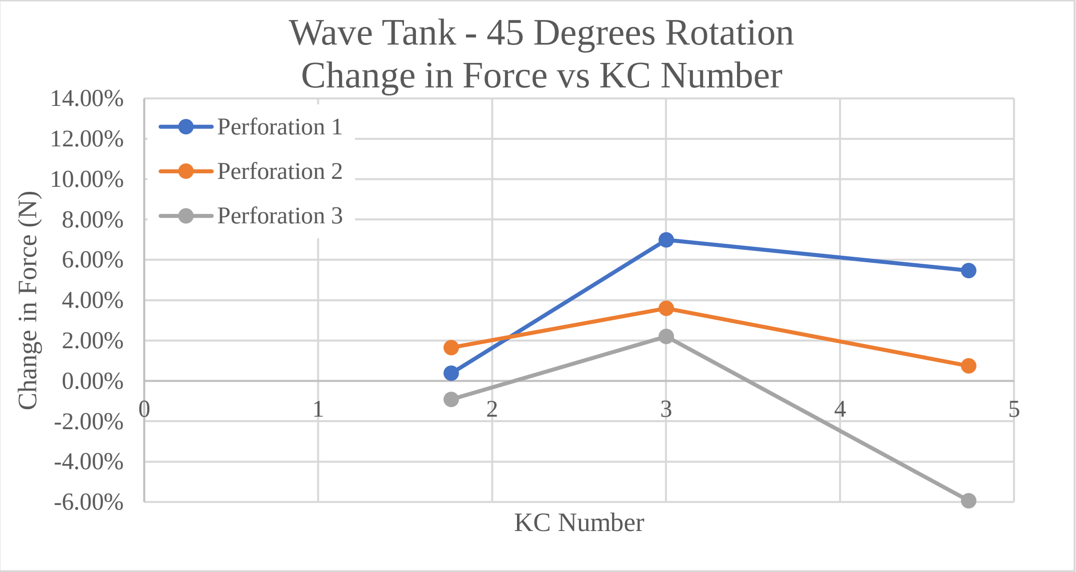

Figure 52: Percent change in wave tank peak force from average for each perforation for a rotation of 45 degrees against the KC number of tested waves

The observations from the CFD analysis do not apply to the wave tank analysis. For the wave tank analysis similar trends can be seen for perforation 1 and 2 while perforation 3 only followed the trends shown by perforation 1 and 2 at 30° and 45° of rotation. A two-sided T-test is performed for the wave tank data to determine the statistical significance of the difference due to rotation. The p-values generated by the test, Table 20, are all greater than 0.05 showing no statistical significance to the orientation of the monopile in relation to an on-coming wave. The CFD data shows an even smaller percent difference to the 0-degree rotation than the difference observed from the wave tank data and is therefore also statistically insignificant.

Table 20: P-Values from two-sided t-test on wave tank results for a given perforation, test wave and rotation.

Perforation	Wave	Rotation	P-Value
1	1	15	0.250
		30	0.144
		45	0.385
	2	15	0.181
		30	0.219
		45	0.277
	3	15	0.203
		30	0.426
		45	0.272
2	1	15	0.053
		30	0.447
		45	0.211
	2	15	0.124
		30	0.288
		45	0.466
	3	15	0.246
		30	0.231
		45	0.268
3	1	15	0.414
		30	0.084
		45	0.404
	2	15	0.322
		30	0.349
		45	0.159
	3	15	0.234
		30	0.272
		45	0.286

Chapter 4

Discussion

Analysis of Results

Determining the effect of a change in approach angle of an oncoming wave required the validation of the CFD simulation results and the scaled physical model test results. The force reductions produced by the CFD simulations are closely relatable to previous research with an R^2 value of 0.7877 or greater. The wave tank results proved to be slightly further from previous research but still centered around the same general line of best fit. The R^2 values from the wave tank line of best fit range between 0.7062 and 0.8901 when compared to previous research by Andersen, et al. (2020) and Ploeg (2021). A direct comparison of forces for test wave #2 shows that the CFD simulations produced forces 3.4% under that of Andersen, et al. (2020) and the wave tank produced forces 5.9% under those produced by Andersen, et al. (2020). With the produced forces from being within 10% between the wave tank physical models, CFD simulations and previous research analysis of the effect of rotation on the force reduction of each perforation began.

The orientation of the monopile against on-coming waves does produce a noticeable difference, both in the wave tank and in the CFD simulations. While the difference is noticeable it does not follow a specific pattern nor is the difference consistent between the CFD simulation data and the wave tank results. While there isn’t a specific correlation, both the CFD simulation data and physical model results show that the 0-degree and 30-degree rotations would be the most optimal for the majority of the test waves. The 0-degree and 30-degree rotations are the most optimal cases for oncoming waves as they show the most benefit without larger increases in force such as those seen in the 15-degree and 45-degree rotations.

The consistent reduction and smaller average deviations in force for the 0-degree and 30-degree rotations is due to the on-coming wave being lined up with a column of perforations. The 0-degree rotation of the monopile lines up the major column of perforations containing 5 perforations with the on-coming wave with a perforation centered at the waterline. The 30-degree rotation of the monopile lines up the minor column of perforations containing 4 perforations with the on-coming wave with the waterline centered between perforations. This placement allows for the crest of test wave #2 to hit the top of a perforation in the major column or the bottom of a perforation in the minor column. Both the wave tank analysis and CFD analysis show that the 0-degree rotation is more optimal than the 30-degree rotation for test wave #2 with the highest KC number, highest wave height and largest force. The 0-degree rotation shows the largest decreases in force for test wave #2 out of each of the rotations without showing a large increase in force for another wave. It should be noted that the largest observed deviation in force was only 12% which is founded statistically insignificant from p-values gather using a two-sided t-test.

Key differences in the plots likely stem from the perforation geometry as the horizontal space left between monopiles decreases with perforation #3. While this does not place a column of perforations in line with the on-coming wave it still provides a passageway for part of the on-coming wave through the monopile.

Sources of Error, Limitations and Suggestions

The first source of error is the methodology of pulling force data from the wave tank tests. While the multipoint calibration allowed the center of force to be variable as the wave passed the load cell the center of force was calculated via numerical analysis given the observed wave parameters of a specific wave. This allowed for an approximation of the center of force at a given time stamp and accounted for any likely phase shift, however it assumes that the max force occurs at the point of max strain recorded in the load cell and that the lowest force occurs at the trough in the recorded strain. A simpler method of data recording and analysis could be achieved by using two sets of wheatstone strain gauge bridges to allow for comparison of the raw strain to determine the moment and subsequently the moment arm for the center of force at a given moment. Additionally, if a single wheatstone bridge is to be continued a methodology of recording pressure under the wave at given z values should be added to reduce errors due to theoretical calculations.

A secondary source of error is the inaccuracy of waves produced in the wave tank. The waves produced both by the piston and hinge wave generators were inconsistent from run to run with the same initial conditions. As a result, multiple runs were conducted for each test to ensure that the differences from run to run could be averaged out, however while this limited errors due to this issue it should not be disregarded completely. The inaccuracy in the waves may also be due to the reflection within the wave tank itself. This could be limited by increasing the sloped media at the end of the tank to create a more porous surface for wave dissipation. The reflection may also be limited by adding wave vanes to the tank to ensure no reflection occurs in the first wave prior to interaction with the monopile.

Future Research

Additional testing of an expanded number of perforations and test waves would allow for a clearer picture to form about the relation of perforation size and direction of an on-coming wave. The additional geometry should add length or width independently of each other to allow for a clear depiction of how and where the wave is hitting the monopile and the effect of the perforation size on the result. In the future this could be combined with stress analysis software to determine if there is an additional benefit to rotating the monopile. Possible benefits could include being able to expand the sizes of the perforations while limiting the stresses that form directly between the perforations.

Chapter 5

Conclusion

CFD analysis was proven to be useful in analysis of perforated monopiles with results within 10% of physical models and within 5% of previous research. The simulations confirmed wave loads are reduced by use of perforations around the waterline with the force reduction increasing with the size of the perforations. The computational fluid dynamics and scaled physical model used in this study showed finite differences ranging from -4% to 12% in force due to the change in direction of an incident wave. Due to the results being near the limits of error between the models, a two-tailed T-test was used to determine statistical significance. It was concluded the orientation of the monopile is not statistically insignificant and should not be a major design consideration as all p-values were above 0.05.

Moving forward, further research is needed to expand the scope of wave regimes and test various perforation geometries and spacing. By systematically analyzing the effects of perforation size, shape, and orientation, future studies can identify the most efficient pattern of perforations to optimize hydrodynamic performance. The expansion in range of analyzed waves will allow for the application of orientation of the monopile in the design of offshore wind turbines.

While previous research has been conducted it served to prove the concept of mitigation of hydrodynamic loads through perforations about the waterline and the limitations of perforation geometries based on fatigue limits set by DNVGL for offshore wind turbines. Andersen, et al. (2020) tested a wide range of wave cases for only one perforation geometry with a reference monopile. The number of perforations was expanded by Ploeg (2021) with the addition of a stress analysis to show that the remaining material between perforations shows an increase in stresses and eventually fails per the DNVGL design limits. The research is further elaborated by Santamaria Gonzalez (2023) by including additional factors such as wind conditions, return periods of wave characteristics, soil conditions and power conditions. An expansion of geometries and variation in spacing could lead towards design standards being developed to allow for use of perforated monopiles in offshore wind farms.

Another future consideration is the effect of biological growth on the interior of the monopile (Maher, et. al., 2018 and Paluzzi, 2023). While the additional area for growth would be beneficial to the environment it may also lead to growth around the perforations. Biological growth may result in a reduction in perforation area and therefore a deterioration in the benefit of the perforations in relation to force reduction.

By integrating perforations, offshore wind facilities' design can mitigate hydrodynamic loading on the monopiles while facilitating the use of standard corrosion protection measures. This dual approach, combining load reduction and protective measures, promises to bolster the reliability and lifespan of offshore wind energy infrastructure.

References

Andersen, J., Abrahamsen, R., Andersen, T., Andersen, M., Baun, T., & Neubauer, J. (2020). Wave Load Mitigation by Perforation of Monopiles. *Journal of Marine Science and Engineering*, *8*(5), 352. https://doi.org/10.3390/jmse8050352

Bakker A. (2008) Lectures on Applied Computational Fluid Dynamics. www.bakker.org.

Bustamante, A., Vera-Tudela, L., & Kühn, M. (2015). Evaluation of wind farm effects on fatigue loads of an individual wind turbine at the EnBW baltic 1 offshore wind farm. *Journal of Physics: Conference Series*, *625*, 012020. https://doi.org/10.1088/1742-6596/625/1/012020

Chakrabarti SK. Hydrodynamics of offshore structures. Springer Verlag;1987.

Christiansen, R. (2020). Living Docks: Structural Implications and Determination of Force Coefficients of Oyster Mats on Dock Pilings in the Indian River Lagoon [Master's Thesis, Florida Institute of Technology].

Clauss, G. (1992). Offshore Structures, Volume 1, Conceptual Design and Hydromechanics. Springer, London, UK.

COMSOL Multiphysics® v. 6.1. www.comsol.com. COMSOL AB, Stockholm, Sweden.

Delwiche, A. & Tavares, I. (2017). Retrofit Strategy using Aluminum Anodes for the Internal section of Windturbine Monopiles. *NACE International Corrosion Conference & Expo*, Paper no. 8955.

Det Norske Veritas (2014) Fatigue design of offshore steel structures. Norway.

Det Norske Veritas (1989). Rules for the Classification of Fixed Offshore Installations. Technical report, DNV, Hovik, Norway.

DNV. (2011). DNV-RP-C203 Fatigue Design of Offshore Steel Structures (tech. rep.). http://www.dnv.com

Elger, D. F., LeBret, B. A., Crowe, C. T., & Roberson, J. A. (2022). *Engineering fluid mechanics*. John Wiley & Sons, Inc.

FLOW-3D® Version 12.0 Users Manual (2018). FLOW-3D [Computer software]. Santa Fe, NM: Flow Science, Inc. https://www.flow3d.com

Gaertner, Evan, Jennifer Rinker, Latha Sethuraman, Frederik Zahle, Benjamin Andersen, Garrett Barter, Nikhar Abbas, Fanzhong Meng, Pietro Bortolotti, Witold Skrzypinski, George Scott, Roland Feil, Henrik Bredmose, Katherine Dykes, Matt Shields, Christopher Allen, and Anthony Viselli. (2020). Definition of the IEA 15-Megawatt Offshore Reference Wind. Golden, CO: National Renewable Energy Laboratory. NREL/TP-5000-75698. https://www.nrel.gov/docs/fy20osti/75698.pdf

Goodisman, Jerry (2001). "Observations on Lemon Cells". Journal of Chemical Education. 78 (4): 516–518. Bibcode:2001JChEd..78..516G. doi:10.1021/ed078p516. Goodisman notes that many chemistry textbooks use an incorrect model for a cell with zinc and copper electrodes in an acidic electrolyte

Hilbert, L.R. & Black, Anders & Andersen, F. & Mathiesen, Troels. (2011). Inspection and monitoring of corrosion inside monopile foundations for offshore wind turbines. European Corrosion Congress 2011, EUROCORR 2011. 3. 2187-2201.

H. J. Landau, "Sampling, data transmission, and the Nyquist rate," in Proceedings of the IEEE, vol. 55, no. 10, pp. 1701-1706, Oct. 1967, doi: 10.1109/PROC.1967.5962.

Journee, J. M., and W. W. Massie. Offshore Hydrodynamics, First Edition. Delft University of Technology, 2001.

Keulegan, G. H., and L. H. Carpenter. “Forces on Cylinders and Plates in an Oscillating Fluid.” Journal of Research of the National Bureau of Standards, vol. 60, no. 5, 1958, pp. 423–40.

Lahlou, O. (2019). Experimental and Numerical Analysis of the Drag Force on Surfboards with Different Shapes (thesis).

L. H. Holthuijsen. Waves in Oceanic and Coastal Waters. Cam-bridge University Press, 2007. doi:10.1017/cbo9780511618536.

MacCamy, R.C., Fuchs, R.A.: Wave Forces on Piles: a Diffraction Theory. Corps of Engineers Washington DC Beach Erosion Board (1954)

M. M. Maher and G. Swain, "The Corrosion and Biofouling Characteristics of Sealed vs. Perforated Offshore Monopile Interiors Experiment Design Comparing Corrosion and Environment Inside Steel Pipe," OCEANS 2018 MTS/IEEE Charleston, Charleston, SC, USA, 2018, pp. 1-4, doi: 10.1109/OCEANS.2018.8604522.

Morison, J. R.; O'Brien, M. P.; Johnson, J. W.; Schaaf, S. A. (1950), "The force exerted by surface waves on piles", Petroleum Transactions, American Institute of Mining Engineers, 189 (5): 149–154, doi:10.2118/950149-G

Paluzzi, Alexander John, "Effects of Perforations on Internal Cathodic Protection and Recruitment of Marine Organisms to Steel Pipes" (2023). Theses and Dissertations. 1403. https://repository.fit.edu/etd/1403

Ploeg, J.V.D. (2021). Perforation of monopiles to reduce hydrodynamic loads and enable use in deep waters [Master’s Thesis, Delft University of Technology] Institutional Repository at Delft University of Technology. http://resolver.tudelft.nl/uuid:91eada6f-4f2b-4ae6-be59-2b5ff0590c6f.

Shi, W., Zhang, S., Michailides, C., Zhang, L., Zhang, P., & Li, X. (2023). Experimental investigation of the hydrodynamic effects of breaking waves on monopiles in model scale. Journal of Marine Science and Technology, 28(1), 314–325. https://doi.org/10.1007/s00773-023-00926-9

Santamaria Gonzalez, G.A. (2023) Advantages and Challenges of Perforated Monopiles in Deep Water Sites [Master's Thesis, Delft University of Technology] Institutional Repository at Delft University of Technology. http://resolver.tudelft.nl/uuid:490791b6-a912-4bac-a007-f77012c01107

Sarpkaya, T. and Isaacson, M. (1981). Mechanics of Wave Forces on Offshore Structures. Number ISBN 0-442-25402-4. Van Nostrand Reinhold Company Inc., New York.

Tang, Y., Shi, W., Ning, D., You, J., & Michailides, C. (2020). Effects of spilling and plunging type breaking waves acting on large monopile offshore wind turbines. Frontiers in Marine Science, 7. https://doi.org/10.3389/fmars.2020.00427

Teja, R. (2021, June 25). Wheatstone bridge: Working, examples, applications. ElectronicsHub. https://www.electronicshub.org/wheatstone-bridge/

The MathWorks Inc. (2022). MATLAB version: 9.13.0 (R2022b), Natick, Massachusetts: The MathWorks Inc. https://www.mathworks.com

Wave gauges. Edinburgh Designs. (2016). http://www4.edesign.co.uk/product/wavegauges/

Wilberts, F. (2017). MEASUREMENT DRIVEN FATIGUE ASSESSMENT OF OFFSHORE WIND TURBINE FOUNDATIONS (Master's Thesis, Uppsala University).

Appendix A: Raw Data from Wave Tank Testing

Reference						
Test Wave #	Run Number	Wave Gauge Number	Wave Height (m)	Wave Period (s)	Wave Length (m)	Force (N)
1	1	1	0.0634	0.8574	1.1301	7.4705
1	1	2	0.0635	0.8541	1.1221	
1	1	3	0.0578	0.8550	1.1243	
1	2	1	0.0622	0.8565	1.1280	8.2455
1	2	2	0.0691	0.8535	1.1206	
1	2	3	0.0603	0.8535	1.1206	
1	3	1	0.0662	0.8606	1.1379	7.9956
1	3	2	0.0702	0.8573	1.1300	
1	3	3	0.0631	0.8570	1.1292	
2	1	1	0.0978	1.7110	3.1873	9.1952
2	1	2	0.1006	1.7180	3.2032	
2	1	3	0.1011	1.7110	3.1873	
2	2	1	0.1026	1.6870	3.1337	12.3342
2	2	2	0.1060	1.6560	3.0626	
2	2	3	0.1056	1.6720	3.0993	
2	3	1	0.0988	1.7190	3.2055	8.2895
2	3	2	0.1023	1.7190	3.2055	
2	3	3	0.1015	1.7030	3.1691	
3	1	1	0.0443	2.6800	5.3224	2.2538
3	1	2	0.0440	2.6410	5.2424	
3	1	3	0.0438	2.7110	5.3936	
3	2	1	0.0480	2.3990	4.7174	3.0540
3	2	2	0.0484	2.4850	4.9009	
3	2	3	0.0480	2.4840	4.8987	
3	3	1	0.0476	2.3830	4.6823	3.1681
3	3	2	0.0486	2.4690	4.8698	
3	3	3	0.0478	2.4690	4.8698	

Perforation #1

Test Wave #	Rotation (deg)	Run Number	Wave Gauge Number	Wave Height (m)	Wave Period (s)	Wave Length (m)	Force (N)
1	0	1	1	0.0581	0.8568	1.1287	6.7738
1	0	1	2	0.0663	0.8545	1.1231	
1	0	1	3	0.0577	0.8535	1.1206	
1	0	2	1	0.0587	0.8574	1.1302	6.6618
1	0	2	2	0.0664	0.8581	1.1319	
1	0	2	3	0.0590	0.8558	1.1262	
1	0	3	1	0.0593	0.8589	1.1338	6.6461
1	0	3	2	0.0668	0.8585	1.1328	
1	0	3	3	0.0632	0.8563	1.1276	
1	15	1	1	0.0598	0.8574	1.1302	6.6893
1	15	1	2	0.0685	0.8574	1.1302	
1	15	1	3	0.0555	0.8546	1.1234	
1	15	2	1	0.0648	0.8599	1.1364	6.6719
1	15	2	2	0.0718	0.8599	1.1364	
1	15	2	3	0.0705	0.8596	1.1357	
1	15	3	1	0.0616	0.8594	1.1350	6.6147
1	15	3	2	0.0696	0.8589	1.1340	
1	15	3	3	0.0612	0.8585	1.1329	
1	30	1	1	0.0613	0.8579	1.1315	6.6800
1	30	1	2	0.0729	0.8580	1.1317	
1	30	1	3	0.0603	0.8580	1.1317	
1	30	2	1	0.0625	0.8594	1.1351	6.9832
1	30	2	2	0.0744	0.8562	1.1272	
1	30	2	3	0.0568	0.8570	1.1292	
1	30	3	1	0.0601	0.8572	1.1297	6.7934
1	30	3	2	0.0728	0.8573	1.1299	
1	30	3	3	0.0574	0.8548	1.1239	
1	45	1	1	0.0632	0.8602	1.1371	6.7190
1	45	1	2	0.0719	0.8594	1.1351	
1	45	1	3	0.0648	0.8586	1.1330	
1	45	2	1	0.0616	0.8594	1.1350	6.8360
1	45	2	2	0.0719	0.8594	1.1351	
1	45	2	3	0.0609	0.8581	1.1318	
1	45	3	1	0.0590	0.8594	1.1351	6.6022

1	45	3	2	0.0698	0.8574	1.1302	
1	45	3	3	0.0601	0.8554	1.1253	
2	0	1	1	0.0930	1.7820	3.3499	6.6301
2	0	1	2	0.0935	1.8200	3.4342	
2	0	1	3	0.0933	1.7890	3.3644	
2	0	2	1	0.1045	1.6720	3.0993	8.5244
2	0	2	2	0.1073	1.6330	3.0088	
2	0	2	3	0.1072	1.6330	3.0088	
2	0	3	1	0.1011	1.6880	3.1360	7.9859
2	0	3	2	0.1027	1.6960	3.1532	
2	0	3	3	0.1036	1.6870	3.1337	
2	15	1	1	0.1008	1.7030	3.1691	7.7808
2	15	1	2	0.1036	1.7110	3.1873	
2	15	1	3	0.1016	1.7030	3.1691	
2	15	2	1	0.1037	1.6640	3.0809	8.2225
2	15	2	2	0.1097	1.6410	3.0271	
2	15	2	3	0.1072	1.6410	3.0271	
2	15	3	1	0.1019	1.6960	3.1532	9.4895
2	15	3	2	0.1104	1.6410	3.0271	
2	15	3	3	0.1033	1.6570	3.0649	
2	30	1	1	0.1009	1.7030	3.1691	7.7108
2	30	1	2	0.1039	1.6950	3.1509	
2	30	1	3	0.1024	1.7030	3.1691	
2	30	2	1	0.1044	1.6560	3.0626	8.4166
2	30	2	2	0.1100	1.6560	3.0626	
2	30	2	3	0.1071	1.6480	3.0442	
2	30	3	1	0.1032	1.6720	3.0993	8.7211
2	30	3	2	0.1137	1.6250	2.9905	
2	30	3	3	0.1089	1.6250	2.9905	
2	45	1	1	0.1032	1.6790	3.1154	8.1794
2	45	1	2	0.1039	1.6950	3.1509	
2	45	1	3	0.1048	1.6800	3.1177	
2	45	2	1	0.1030	1.6720	3.0993	8.4573
2	45	2	2	0.1059	1.6480	3.0442	
2	45	2	3	0.1056	1.6490	3.0465	
2	45	3	1	0.1001	1.7040	3.1714	7.7688
2	45	3	2	0.1032	1.7180	3.2032	
2	45	3	3	0.1023	1.6950	3.1509	

3	0	1	1	0.0483	2.4060	4.7327	3.1466
3	0	1	2	0.0510	2.4920	4.9160	
3	0	1	3	0.0481	2.4690	4.8698	
3	0	2	1	0.0419	2.5550	5.0525	3.2235
3	0	2	2	0.0520	2.4610	4.8523	
3	0	2	3	0.0498	2.4850	4.9009	
3	0	3	1	0.0461	2.3910	4.6998	2.8476
3	0	3	2	0.0481	2.4770	4.8836	
3	0	3	3	0.0473	2.4840	4.8987	
3	15	1	1	0.0470	2.3980	4.7152	2.9439
3	15	1	2	0.0486	2.4610	4.8523	
3	15	1	3	0.0470	2.4850	4.9009	
3	15	2	1	0.0472	2.3980	4.7152	2.9742
3	15	2	2	0.0502	2.4680	4.8676	
3	15	2	3	0.0477	2.4840	4.8987	
3	15	3	1	0.0467	2.4070	4.7349	2.9394
3	15	3	2	0.0515	2.4920	4.9160	
3	15	3	3	0.0489	2.4840	4.8987	
3	30	1	1	0.0503	2.4300	4.7813	3.1580
3	30	1	2	0.0536	2.4530	4.8348	
3	30	1	3	0.0515	2.4760	4.8851	
3	30	2	1	0.0461	2.3750	4.6648	3.0763
3	30	2	2	0.0493	2.4770	4.8836	
3	30	2	3	0.0471	2.4850	4.9009	
3	30	3	1	0.0464	2.4370	4.7965	2.8997
3	30	3	2	0.0490	2.4840	4.8987	
3	30	3	3	0.0458	2.4530	4.8348	
3	45	1	1	0.0506	2.4220	4.7640	3.2108
3	45	1	2	0.0543	2.4450	4.8173	
3	45	1	3	0.0516	2.4610	4.8523	
3	45	2	1	0.0469	2.4220	4.7640	2.8206
3	45	2	2	0.0475	2.4530	4.8348	
3	45	2	3	0.0459	2.4690	4.8698	
3	45	3	1	0.0533	2.4530	4.8348	3.8309
3	45	3	2	0.0586	2.5000	4.9333	
3	45	3	3	0.0562	2.5470	5.0353	

Perforation #2							
Test Wave #	Rotation (deg)	Run Number	Wave Gauge Number	Wave Height (m)	Wave Period (s)	Wave Length (m)	Force (N)
1	0	1	1	0.0604	0.8600	1.1366	5.2443
1	0	1	2	0.0655	0.8594	1.1350	
1	0	1	3	0.0624	0.8588	1.1335	
1	0	2	1	0.0604	0.8594	1.1350	5.5303
1	0	2	2	0.0664	0.8579	1.1314	
1	0	2	3	0.0582	0.8558	1.1263	
1	0	3	1	0.0568	0.8594	1.1351	5.3545
1	0	3	2	0.0637	0.8587	1.1333	
1	0	3	3	0.0554	0.8581	1.1319	
1	15	1	1	0.0566	0.8576	1.1306	5.7178
1	15	1	2	0.0665	0.8559	1.1265	
1	15	1	3	0.0535	0.8559	1.1265	
1	15	2	1	0.0581	0.8594	1.1352	5.5763
1	15	2	2	0.0654	0.8559	1.1265	
1	15	2	3	0.0602	0.8550	1.1243	
1	15	3	1	0.0561	0.8593	1.1348	5.4940
1	15	3	2	0.0644	0.8555	1.1255	
1	15	3	3	0.0555	0.8531	1.1197	
1	30	1	1	0.0578	0.8551	1.1245	5.5527
1	30	1	2	0.0688	0.8565	1.1281	
1	30	1	3	0.0557	0.8551	1.1245	
1	30	2	1	0.0590	0.8594	1.1350	5.3265
1	30	2	2	0.0690	0.8585	1.1328	
1	30	2	3	0.0603	0.8585	1.1328	
1	30	3	1	0.0605	0.8606	1.1379	5.2993
1	30	3	2	0.0703	0.8594	1.1351	
1	30	3	3	0.0633	0.8591	1.1343	
1	45	1	1	0.0574	0.8578	1.1312	5.5095
1	45	1	2	0.0670	0.8570	1.1292	
1	45	1	3	0.0572	0.8562	1.1272	
1	45	2	1	0.0578	0.8565	1.1281	5.5127
1	45	2	2	0.0661	0.8563	1.1275	
1	45	2	3	0.0577	0.8547	1.1236	
1	45	3	1	0.0566	0.8580	1.1317	5.3724

1	45	3	2	0.0664	0.8580	1.1317	
1	45	3	3	0.0534	0.8558	1.1263	
2	0	1	1	0.1048	1.6640	3.0809	7.4599
2	0	1	2	0.1126	1.6490	3.0465	
2	0	1	3	0.1069	1.6400	3.0249	
2	0	2	1	0.1010	1.7030	3.1691	6.6839
2	0	2	2	0.1066	1.7190	3.2055	
2	0	2	3	0.1024	1.7030	3.1691	
2	0	3	1	0.1031	1.6720	3.0993	7.1722
2	0	3	2	0.1105	1.6560	3.0626	
2	0	3	3	0.1056	1.6480	3.0442	
2	15	1	1	0.1008	1.7110	3.1873	9.0408
2	15	1	2	0.1106	1.6560	3.0626	
2	15	1	3	0.1036	1.6640	3.0809	
2	15	2	1	0.1043	1.6640	3.0809	7.6111
2	15	2	2	0.1110	1.6490	3.0465	
2	15	2	3	0.1070	1.6400	3.0249	
2	15	3	1	0.1050	1.6640	3.0809	7.2243
2	15	3	2	0.1105	1.6560	3.0626	
2	15	3	3	0.1059	1.6560	3.0626	
2	30	1	1	0.1044	1.6720	3.0993	7.7515
2	30	1	2	0.1130	1.6170	2.9721	
2	30	1	3	0.1078	1.6170	2.9721	
2	30	2	1	0.0977	1.7660	3.3135	6.3083
2	30	2	2	0.1009	1.7810	3.3476	
2	30	2	3	0.0965	1.7730	3.3294	
2	30	3	1	0.0968	1.7340	3.2395	8.7235
2	30	3	2	0.1071	1.7030	3.1691	
2	30	3	3	0.1020	1.6870	3.1337	
2	45	1	1	0.1010	1.6800	3.1177	7.9383
2	45	1	2	0.1111	1.6170	2.9721	
2	45	1	3	0.1056	1.6090	2.9537	
2	45	2	1	0.0980	1.7650	3.3112	6.1725
2	45	2	2	0.1003	1.7970	3.3824	
2	45	2	3	0.0968	1.7730	3.3294	
2	45	3	1	0.1044	1.6710	3.0970	7.3633
2	45	3	2	0.1099	1.6570	3.0649	
2	45	3	3	0.1053	1.6560	3.0626	

3	0	1	1	0.0460	2.3830	4.6823	2.8525
3	0	1	2	0.0495	2.4770	4.8836	
3	0	1	3	0.0477	2.4680	4.8676	
3	0	2	1	0.0467	2.3980	4.7152	2.6525
3	0	2	2	0.0488	2.4690	4.8698	
3	0	2	3	0.0480	2.4840	4.8987	
3	0	3	1	0.0474	2.3750	4.6648	2.6362
3	0	3	2	0.0540	2.4380	4.7986	
3	0	3	3	0.0521	2.4380	4.7986	
3	15	1	1	0.0464	2.3980	4.7152	2.6967
3	15	1	2	0.0490	2.4690	4.8698	
3	15	1	3	0.0471	2.4850	4.9009	
3	15	2	1	0.0475	2.4140	4.7467	2.6305
3	15	2	2	0.0510	2.5000	4.9333	
3	15	2	3	0.0489	2.4760	4.8851	
3	15	3	1	0.0467	2.3980	4.7152	2.6322
3	15	3	2	0.0493	2.4760	4.8851	
3	15	3	3	0.0473	2.4920	4.9160	
3	30	1	1	0.0499	2.4220	4.7640	2.5765
3	30	1	2	0.0495	2.5000	4.9333	
3	30	1	3	0.0499	2.5000	4.9333	
3	30	2	1	0.0474	2.3980	4.7152	2.6520
3	30	2	2	0.0500	2.4600	4.8501	
3	30	2	3	0.0483	2.4770	4.8836	
3	30	3	1	0.0467	2.3980	4.7152	2.7117
3	30	3	2	0.0486	2.4930	4.9182	
3	30	3	3	0.0474	2.4840	4.8987	
3	45	1	1	0.0455	2.3750	4.6648	3.0541
3	45	1	2	0.0503	2.4460	4.8195	
3	45	1	3	0.0479	2.4450	4.8173	
3	45	2	1	0.0458	2.3830	4.6823	2.6922
3	45	2	2	0.0486	2.4760	4.8851	
3	45	2	3	0.0481	2.4450	4.8173	
3	45	3	1	0.0451	2.4060	4.7327	2.6875
3	45	3	2	0.0480	2.4690	4.8698	
3	45	3	3	0.0476	2.4770	4.8836	

Perforation #3							
Test Wave #	Rotation (deg)	Run Number	Wave Gauge Number	Wave Height (m)	Wave Period (s)	Wave Length (m)	Force (N)
1	0	1	1	0.0580	0.8599	1.1364	3.8176
1	0	1	2	0.0595	0.8574	1.1303	
1	0	1	3	0.0579	0.8589	1.1338	
1	0	2	1	0.0561	0.8587	1.1333	3.8229
1	0	2	2	0.0588	0.8568	1.1286	
1	0	2	3	0.0535	0.8568	1.1286	
1	15	1	1	0.0562	0.8573	1.1299	3.7480
1	15	1	2	0.0594	0.8574	1.1302	
1	15	1	3	0.0545	0.8574	1.1302	
1	15	2	1	0.0570	0.8604	1.1375	3.8180
1	15	2	2	0.0603	0.8583	1.1324	
1	15	2	3	0.0553	0.8588	1.1336	
1	15	3	1	0.0586	0.8607	1.1384	3.7668
1	15	3	2	0.0604	0.8583	1.1324	
1	15	3	3	0.0598	0.8572	1.1298	
1	30	1	1	0.0557	0.8558	1.1263	3.7835
1	30	1	2	0.0615	0.8558	1.1263	
1	30	1	3	0.0548	0.8565	1.1281	
1	30	2	1	0.0565	0.8604	1.1375	3.7532
1	30	2	2	0.0622	0.8573	1.1300	
1	30	2	3	0.0550	0.8583	1.1325	
1	30	3	1	0.0567	0.8608	1.1386	3.7420
1	30	3	2	0.0608	0.8558	1.1263	
1	30	3	3	0.0576	0.8573	1.1299	
1	45	1	1	0.0555	0.8577	1.1308	3.7371
1	45	1	2	0.0600	0.8550	1.1243	
1	45	1	3	0.0534	0.8568	1.1287	
1	45	2	1	0.0575	0.8579	1.1313	3.7661
1	45	2	2	0.0613	0.8569	1.1291	
1	45	2	3	0.0578	0.8584	1.1327	
1	45	3	1	0.0556	0.8562	1.1272	3.8526
1	45	3	2	0.0613	0.8562	1.1272	
1	45	3	3	0.0488	0.8554	1.1253	
2	0	1	1	0.1051	1.6560	3.0626	6.1543

2	0	1	2	0.1123	1.6090	2.9537	
2	0	1	3	0.1064	1.6180	2.9744	
2	0	2	1	0.1026	1.6800	3.1177	5.6740
2	0	2	2	0.1082	1.6870	3.1337	
2	0	2	3	0.1023	1.6800	3.1177	
2	0	3	1	0.0994	1.6870	3.1337	6.2884
2	0	3	2	0.1058	1.6570	3.0649	
2	0	3	3	0.0991	1.6410	3.0271	
2	15	1	1	0.1011	1.6950	3.1509	5.4872
2	15	1	2	0.1061	1.7110	3.1873	
2	15	1	3	0.1003	1.7030	3.1691	
2	15	2	1	0.0989	1.6720	3.0993	6.3275
2	15	2	2	0.1057	1.6250	2.9905	
2	15	2	3	0.0975	1.6330	3.0088	
2	15	3	1	0.1052	1.6640	3.0809	5.8415
2	15	3	2	0.1101	1.6560	3.0626	
2	15	3	3	0.1022	1.6560	3.0626	
2	30	1	1	0.0973	1.6870	3.1337	6.2518
2	30	1	2	0.1054	1.6410	3.0271	
2	30	1	3	0.0981	1.6400	3.0249	
2	30	2	1	0.1045	1.6410	3.0271	6.0256
2	30	2	2	0.1125	1.6170	2.9721	
2	30	2	3	0.1086	1.6090	2.9537	
2	30	3	1	0.0970	1.6790	3.1154	6.1060
2	30	3	2	0.1034	1.6330	3.0088	
2	30	3	3	0.0994	1.6400	3.0249	
2	45	1	1	0.0983	1.7350	3.2418	5.1776
2	45	1	2	0.1031	1.7580	3.2953	
2	45	1	3	0.0978	1.7350	3.2418	
2	45	2	1	0.1054	1.6560	3.0626	5.8778
2	45	2	2	0.1103	1.6560	3.0626	
2	45	2	3	0.1035	1.6560	3.0626	
2	45	3	1	0.1041	1.6640	3.0809	5.9865
2	45	3	2	0.1134	1.6250	2.9905	
2	45	3	3	0.1074	1.6250	2.9905	
3	0	1	1	0.0457	2.3990	4.7174	2.1719
3	0	1	2	0.0486	2.4770	4.8836	
3	0	1	3	0.0467	2.4770	4.8836	

3	0	2	1	0.0460	2.4060	4.7327	2.0077
3	0	2	2	0.0495	2.4840	4.8987	
3	0	2	3	0.0464	2.4930	4.9182	
3	0	3	1	0.0464	2.4060	4.7327	2.1025
3	0	3	2	0.0484	2.4930	4.9182	
3	0	3	3	0.0469	2.4760	4.8851	
3	15	1	1	0.0458	2.3510	4.6095	2.3942
3	15	1	2	0.0498	2.4300	4.7813	
3	15	1	3	0.0478	2.4370	4.7965	
3	15	2	1	0.0464	2.4060	4.7327	2.0663
3	15	2	2	0.0485	2.4840	4.8987	
3	15	2	3	0.0466	2.4840	4.8987	
3	15	3	1	0.0459	2.3820	4.6801	2.1051
3	15	3	2	0.0497	2.4610	4.8523	
3	15	3	3	0.0475	2.4770	4.8836	
3	30	1	1	0.0465	2.3980	4.7152	2.0658
3	30	1	2	0.0485	2.4850	4.9009	
3	30	1	3	0.0471	2.4920	4.9160	
3	30	2	1	0.0466	2.3910	4.6998	2.0652
3	30	2	2	0.0479	2.4930	4.9182	
3	30	2	3	0.0473	2.4920	4.9160	
3	30	3	1	0.0458	2.4060	4.7327	2.0470
3	30	3	2	0.0492	2.4920	4.9160	
3	30	3	3	0.0475	2.4850	4.9009	
3	45	1	1	0.0458	2.4070	4.7349	2.2483
3	45	1	2	0.0489	2.4920	4.9160	
3	45	1	3	0.0477	2.5080	4.9505	
3	45	2	1	0.0458	2.3980	4.7152	2.1209
3	45	2	2	0.0486	2.4760	4.8851	
3	45	2	3	0.0467	2.4770	4.8836	
3	45	3	1	0.0466	2.3990	4.7174	2.0512
3	45	3	2	0.0479	2.4920	4.9160	
3	45	3	3	0.0473	2.4840	4.8987	

Appendix B: Comparison Table of Wave Tank results and CFD Analysis Based on Observed Wave Tank Parameters

	Monopile	Wave Tank Results			CFD Results 2			
		H (m)	T (s)	L (m)	H (m)	T (s)	L (m)	Height Dif (m)
Wave #1	Reference	0.0604	0.85813	4.41508	0.0638	0.8563	1.127537751	-0.003
	Perforation #1	0.0608	0.85861	1.98114	0.0618	0.8399	1.087505769	-0.001
	Perforation #2	0.0576	0.85855	1.96174	0.0607	0.8398	1.087204621	-0.003
	Perforation #3	0.0567	0.85871	2.03236	0.0594	0.8569	1.129038742	-0.003
Wave #2	Reference	0.0997	1.7057	2.7695	0.1147	1.6033	2.94050079	-0.015
	Perforation #1	0.1017	1.7069	3.8155	0.1082	1.6379	3.019951636	-0.007
	Perforation #2	0.1018	1.6972	3.8153	0.1073	1.6381	3.020390671	-0.006
	Perforation #3	0.1016	1.6763	3.7723	0.1075	1.6705	3.095881644	-0.006
Wave #3	Reference	0.0466	2.4873	0.8579	0.0457	2.3681	4.646510831	0.001
	Perforation #1	0.0476	2.4245	3.4434	0.0433	2.2682	4.4286128	0.004
	Perforation #2	0.0468	2.3957	3.4115	0.0431	2.2689	4.4300866	0.004
	Perforation #3	0.0461	2.3958	4.7136	0.0471	2.3175	4.539281132	-0.001

Appendix C: Dependency List for Matlab Code

All code and data files may be found at https://github.com/arewyin/Computational-Fluid-Dynamics-Study-of-Perforated-Monopiles.

1. Load_Cell_Calb2.m – Single point-load calibration of load cell
    - importfile2.m
2. Wave_Tank_Analysis_2.m - Runs results from primary testing in wave tank
    - importPerfLoadPath.m
    - importPerfPath.m
    - importRefLoadPath.m
    - importRefPaths.m
    - Load_Cell_Force.m
        - importfile2.m
        - MFCentroid.m
        - StrainZeroCrossings.m
    - R_SQ.m
    - Three_Gauge_Wave_Data.m
        - DataTimeCapGuages.m
        - CapGauge3Import.m
        - ZeroUp.m
    - WaveSolver.m
    - tanhfit.m
3. Wave_Tank_Analysis_3.m - Runs results from secondary testing to match observed wave heights from Andersen, et al. (2020)
    - importRefLoadPath.m
    - importRefPaths.m
    - Load_Cell_Force.m
        - importfile2.m
        - MFCentroid.m
        - StrainZeroCrossings.m
    - Three_Gauge_Wave_Data.m
        - DataTimeCapGuages.m
        - CapGauge3Import.m
        - ZeroUp.m
    - WaveSolver.m

4. Scaled_Analysis.m - Runs results from primary CFD Simulations
    - import01.m
    - importPressAndForce.m
    - R_SQ.m
    - tanhfit.m
5. Scaled_Analysis_WT_Param.m – Runs results from secondary CFD simulations to match observed wave tank parameters and compares with previous wave tank results.
    - import01.m
    - importPressAndForce.m
    - R_SQ.m
    - tanhfit.m
6. Scaled_Analysis_WT_Param_2.m – Runs results from secondary CFD simulations to match observed wave tank parameters and tertiary results to match Andersen, et al. (2020) observed wave parameters for reference monopile in test wave #2.
    - import01.m
    - importPressAndForce.m
    - R_SQ.m
    - tanhfit.m